



ENSO and Pacific Decadal Variability in the Community Climate System Model Version 4

CLARA DESER, ADAM S. PHILLIPS, ROBERT A. TOMAS, AND YUKO M. OKUMURA

Climate and Global Dynamics Division, NCAR, Boulder, Colorado

MICHAEL A. ALEXANDER, ANTONIETTA CAPOTONDI, AND JAMES D. SCOTT

NOAA/Earth System Research Laboratory, Boulder, Colorado

YOUNG-OH KWON

Woods Hole Oceanographic Institution, Woods Hole, Massachusetts

MASAMICHI OHBA

Central Research Institute of Electric Power Industry, Abiko, Japan

(Manuscript received 25 May 2011, in final form 16 September 2011)

ABSTRACT

This study presents an overview of the El Niño–Southern Oscillation (ENSO) phenomenon and Pacific decadal variability (PDV) simulated in a multicentury preindustrial control integration of the NCAR Community Climate System Model version 4 (CCSM4) at nominal 1° latitude–longitude resolution. Several aspects of ENSO are improved in CCSM4 compared to its predecessor CCSM3, including the lengthened period (3–6 yr), the larger range of amplitude and frequency of events, and the longer duration of La Niña compared to El Niño. However, the overall magnitude of ENSO in CCSM4 is overestimated by ~30%. The simulated ENSO exhibits characteristics consistent with the delayed/recharge oscillator paradigm, including correspondence between the lengthened period and increased latitudinal width of the anomalous equatorial zonal wind stress. Global seasonal atmospheric teleconnections with accompanying impacts on precipitation and temperature are generally well simulated, although the wintertime deepening of the Aleutian low erroneously persists into spring. The vertical structure of the upper-ocean temperature response to ENSO in the north and south Pacific displays a realistic seasonal evolution, with notable asymmetries between warm and cold events. The model shows evidence of atmospheric circulation precursors over the North Pacific associated with the “seasonal footprinting mechanism,” similar to observations. Simulated PDV exhibits a significant spectral peak around 15 yr, with generally realistic spatial pattern and magnitude. However, PDV linkages between the tropics and extratropics are weaker than observed.

1. Introduction

The El Niño–Southern Oscillation (ENSO) phenomenon in the tropical Indo-Pacific provides an important source of predictability for interannual climate anomalies worldwide (Ropelewski and Halpert 1987; Philander 1990; Glantz 2000; Tippett and Barnston 2008; and many others). Warm (El Niño) and cold [La Niña

(LN)] phases of ENSO typically last 1–2 yr and repeat approximately every 3–8 yr, with cold events being somewhat weaker and of longer duration than their warm counterparts (e.g., Harrison and Larkin 1998; Okumura and Deser 2010). Driven primarily by coupled ocean–atmosphere processes within the tropical Indo-Pacific basin, the effects of ENSO are transmitted worldwide via atmospheric teleconnections, affecting precipitation and temperature in many societally vulnerable areas (Trenberth et al. 1998; Alexander et al. 2002). Although the basic physical mechanisms of thermal and dynamical air–sea coupling that give rise to ENSO are well studied

Corresponding author address: C. Deser, Climate and Global Dynamics Division, NCAR, P.O. Box 3000, Boulder, CO 80307.
E-mail: cdeser@ucar.edu

(see reviews by Neelin et al. 1998; Wang and Picaut 2004; Chang et al. 2006), other aspects remain less well understood. These include processes responsible for the spatial and temporal asymmetries between El Niño and La Niña, the degree of regularity of the ENSO “cycle,” and triggering mechanisms of warm and cold events.

Coupled ocean–atmosphere models have improved considerably in their simulation of ENSO in past years, becoming realistic enough to be used to explore questions that would be difficult to answer from the short observational record alone. A recent example is the 2000-yr control simulation of the Geophysics Fluid Dynamics Laboratory (GFDL) model (Wittenberg 2009), which exhibits large decadal-to-centennial modulation of ENSO behavior under constant boundary conditions (e.g., fixed greenhouse gas concentrations). Such internal variability implies that identifying externally forced changes in ENSO behavior from the relatively short observational record may have limited success, although paleoclimate proxy records may be useful in this regard (Li et al. 2011). Stevenson et al. (2010) estimate that approximately 250 yr is the minimum record length needed to assess changes in ENSO with 90% confidence.

In addition to interannual ENSO fluctuations, the Indo-Pacific exhibits decadal and multidecadal climate variability (Mantua et al. 1997; Zhang et al. 1997; Deser et al. 2004; Guan and Nigam 2008; Alexander 2010). The most prominent structure of low-frequency climate variability in the North Pacific, with extensions to the tropical Indo-Pacific, has been termed the “Pacific decadal oscillation” (PDO) by Mantua et al. (1997). The PDO is also known as the interdecadal Pacific oscillation (Power et al. 1999) in recognition of its extension to the South Pacific (see also Shakun and Shaman 2009). Given the relatively short observational record, it is difficult to ascertain whether there is a robust spectral peak in the PDO time series. Some studies suggest nominal time scales of approximately 20 and 50 yr (Minobe 1997, 1999; Deser et al. 2004), but most of the variance does not differ significantly from a first-order autoregressive process (e.g., red noise). For this reason, we shall use the terms Pacific decadal variability (PDV) and PDO interchangeably in this study. Other patterns of decadal variability have been identified, for example, the North Pacific mode (Deser and Blackmon 1995; Nakamura et al. 1997; Barlow et al. 2001; Guan and Nigam 2008), the pan-Pacific mode (Guan and Nigam 2008), and the North Pacific gyre oscillation (Di Lorenzo et al. 2008). Investigation of these additional patterns in the Community Climate System Model version 4 (CCSM4) is beyond the scope of this study.

Various mechanisms have been hypothesized to account for PDV, including ENSO and associated atmospheric

teleconnections to the North Pacific, forcing by random fluctuations in the Aleutian low pressure system, oceanic Rossby wave adjustment to wind stress curl variations in the North Pacific, and upper-ocean mixed layer processes (Latif and Barnett 1994; Deser et al. 1999; Pierce 2001; Newman et al. 2003; Vimont 2005; Schneider and Cornuelle 2005; Kwon and Deser 2007; Qiu et al. 2007; Alexander 2010; Shakun and Shaman 2009). The latter includes the so-called “reemergence mechanism” whereby sea surface temperature (SST) anomalies are able to persist from one winter to the next because of the seasonal cycle of upper-ocean mixed layer depth (Alexander and Deser 1995; Alexander et al. 2001). This mechanism acts to impart additional memory to extratropical Pacific SST anomalies beyond that associated with the thermal inertia of a fixed-depth ocean mixed layer (Deser et al. 2003). Coupled models simulate some aspects of PDV, although linkages between the tropical and North Pacific are weaker than observed (Alexander et al. 2006; Kwon and Deser 2007; Zhong et al. 2008).

While the response to ENSO extends from the tropical Pacific to the extratropics, variability originating in the North Pacific may also influence the tropical Pacific via the atmosphere (e.g., Pierce et al. 2000) and the ocean (e.g., Kleeman et al. 1999). Based on analyses of an extended coupled model simulation, Vimont et al. (2001, 2003a) proposed an extratropical-to-tropical connection termed the “seasonal footprinting mechanism” (SFM), where internal fluctuations in the atmospheric circulation over the North Pacific during winter imparts a “footprint” on the ocean through changes in surface heat fluxes. The SST footprint, which peaks in spring and persists through summer in the subtropical Pacific, impacts the atmospheric circulation including zonal wind stress and surface energy fluxes that extend deep into the tropics. These anomalies excite a response in the central and eastern equatorial Pacific Ocean in the subsequent fall and winter that influence ENSO and decadal tropical variability (Vimont et al. 2001, 2003a). Aspects of the SFM and its impact on ENSO have been verified in a number of subsequent observational (Vimont et al. 2003b; Anderson 2003, 2004; Alexander et al. 2008) and modeling studies (Vimont et al. 2009; Zhang et al. 2009; Alexander et al. 2010), including an analysis of CCSM2 (Anderson and Maloney 2006).

The purpose of this study is to provide an overview of ENSO and PDV in the CCSM4, the newest version of the model. We make use of a 1300-yr control integration at nominal 1° resolution under 1850 atmospheric carbon dioxide concentrations; the long record enables us to compute robust statistics of the simulation. We assess the realism of CCSM4 by comparing it to a broad suite of observational atmospheric and oceanic datasets. We also compare

CCSM4 with the previous model version (CCSM3) whose ENSO and PDV have been documented in Deser et al. (2006) and Alexander et al. (2006), respectively.

An interim version of CCSM4, denoted CCSM3.5, was the first version of the model to simulate a credible ENSO period (Neale et al. 2008). This achievement was attributed to changes in the parameterization of tropical atmospheric deep convection as discussed in detail by Neale et al. (2008). Although the frequency characteristics of ENSO are similar between CCSM3.5 and CCSM4, our investigation complements and extends the description of ENSO provided by Neale et al. (2008) for CCSM3.5. In particular, we assess aspects not considered in Neale et al. (2008), including El Niño–La Niña asymmetries, global atmospheric teleconnections, extratropical upper-ocean thermal response, and atmospheric precursors from the North Pacific. Also, CCSM4 provides a longer (1300 yr) control integration than the 80-yr CCSM3.5 simulation examined in Neale et al. (2008), allowing a more robust assessment of ENSO properties and teleconnections.

The rest of the paper is structured as follows. Section 2 provides a brief description of the model and salient changes from CCSM3, as well as a listing of observational datasets used in this study. Section 3 documents ENSO and PDV, addressing the issues discussed above. Section 4 summarizes the results and highlights outstanding issues.

2. Model description and observational datasets

a. CCSM4

The CCSM4 is a state-of-the-art coupled general circulation model comprised of four components (atmosphere, ocean, land, and cryosphere) linked by means of a flux coupler. In this study, we focus on a 1300-yr 1850 control integration of CCSM4 at an atmospheric resolution of 0.9° latitude and 1.25° longitude, hereafter referred to as CCSM4- 1° . We compare the CCSM4- 1° simulation with a multicentury control integration of the previous version of the model, CCSM3, at T85 atmospheric resolution (1.4° latitude and 1.4° longitude). We also briefly examine a multicentury control integration of the 1.8° latitude and 2.5° longitude (atmospheric resolution) version of CCSM4 (denoted CCSM4- 2°).

A brief overview of CCSM4 and salient changes to the atmospheric and oceanic model components is given below. The reader is referred to Gent et al. (2011), Danabasoglu et al. (2012), and R. B. Neale et al. (2011, unpublished manuscript) for additional information. The Community Atmosphere Model, version 4 (CAM4) uses a finite-volume core (Lin 2004) compared to the spectral core in CAM3. The deep convection scheme in CAM4 includes the effects of deep convection in the momentum equation (Richter and Rasch 2008) and uses

a dilute approximation in the plume calculation (Neale et al. 2008), aspects not included in CAM3. The ocean model component has 60 vertical levels as opposed to 40 in CCSM3, with the number of levels in the upper 200 m increased from 14 to 20. It uses spherical coordinates in the Southern Hemisphere and a displaced-pole grid in the Northern Hemisphere. The ocean model resolution, identical for the 1° and 2° versions of CCSM4, is nearly uniform in longitude ($\sim 1.13^\circ$) and variable in latitude (0.27° at the equator, increasing to 0.65° at 60°N in the western North Pacific). See Danabasoglu et al. (2012) for more information on the ocean component of CCSM4.

b. Observational datasets

The following observational datasets are used: 1) sea level pressure (SLP), surface wind components and 300-hPa streamfunction from the National Centers for Environmental Prediction (NCEP)–National Center for Atmospheric Research (NCAR) reanalysis project (Kalnay et al. 1996) during 1957–2008 on a 2.5° grid; 2) SST from the Hadley Centre Sea Ice and SST (HadISST) dataset (Rayner et al. 2003) during 1900–2010 on a 1° grid; 3) air temperature over land from the Hadley Centre–Climatic Research Unit (CRU) surface temperature version 3 (HadCRUT3) dataset (Brohan et al. 2006) during 1957–2008 on a 5° grid; 4) precipitation from the Global Precipitation Climatology Project (GPCP; Adler et al. 2003) based on a blend of satellite and in situ measurements during 1979–2009 on a 2.5° grid; and 5) upper-ocean temperature from the Simple Ocean Data Assimilation (SODA) reanalysis version 2.1.6 for the period 1958–2007 on a 0.5° latitude– 0.5° longitude grid and 40 levels in the vertical (14 in the upper 200 m) (Carton and Giese 2008). The SODA reanalysis is driven by winds from the 40-yr European Centre for Medium-Range Weather Forecasts (ECMWF) Re-Analysis Project (ERA-40).

3. Results

a. ENSO

1) NIÑO-3.4 SST VARIABILITY

The simulation of the climatological annual mean SST distribution in the Indo-Pacific, in particular the strength and zonal extent of the Pacific equatorial cold tongue and western warm pool (SSTs $> 29^\circ\text{C}$), are improved in CCSM4- 1° compared to CCSM4- 2° and CCSM3-T85 with respect to HadISST observations (Fig. 1). The spatial pattern of the standard deviation δ_{SST} of monthly SST anomalies (anomalies are defined as the departures from the long-term monthly means) is realistically simulated in CCSM4- 1° , with maxima along the equatorial

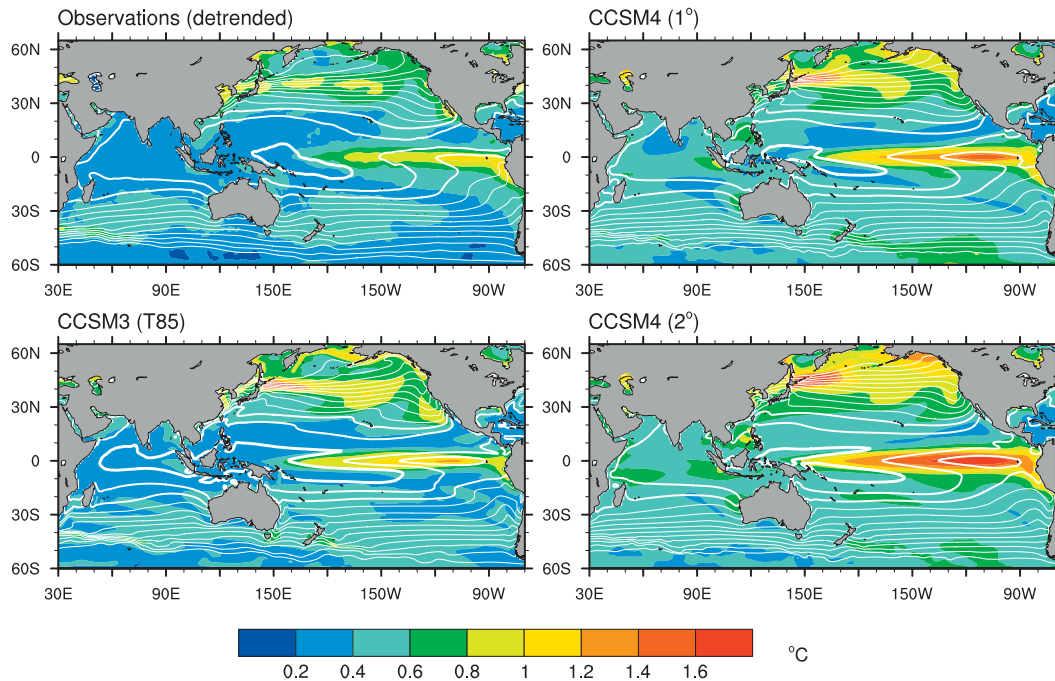


FIG. 1. Climatological annual mean SST (contoured every 2°C beginning at 5°C; the thick contour is 29°C) and standard deviation of monthly SST anomalies (°C, color shading) from (top left) detrended observations (HadISST, 1900–2010) and multicentury preindustrial control integrations of (top right) CCSM4-1°, (bottom left) CCSM3-T85, and (bottom right) CCSM4-2. and.

Pacific cold tongue, along 40°–50°N in the western and central Pacific, and off the west coast of North America (Fig. 1). However, the magnitudes of δ_{SST} in CCSM4-1° are approximately 30% stronger than observed in all 3 regions. In comparison, δ_{SST} in CCSM4-2° is overestimated by at least 70% in these areas. Values of δ_{SST} in CCSM3-T85 are comparable to those in CCSM4-1° over the North Pacific and more realistic than those in CCSM4-1° over the equatorial cold tongue.

A commonly used index for representing SST variability associated with ENSO is the area average of monthly SST anomalies in the region, 5°N–5°S, 170°–120°W, referred to as the “Niño-3.4 index” (see, e.g., Trenberth et al. 2002). This region is located within the area of maximum SST variance and also lies within the center of action of the leading empirical orthogonal function (EOF) pattern of monthly SST anomalies (shown later in Fig. 20a). The monthly Niño-3.4 SST indices from the HadISST observations during 1900–2011 and from each 100-yr segment of the full 1300-yr CCSM4-1° control integration are compared in Fig. 2. Visual inspection of the time series reveals substantial multidecadal modulation of ENSO characteristics (amplitude, duration, and regularity) in CCSM4-1°, reminiscent of that in the GFDL model (Wittenberg 2009). Periods of strong, regular oscillations are apparent such as model years 350–400 (highlighted by the green shading in Fig. 2) as are periods of

weak, irregular fluctuations such as model years 450–499 (highlighted by the yellow shading). There is also evidence of irregularity in the duration of simulated warm and cold events, with some extending over multiple years (e.g., warm events during model years 100–130 highlighted by the red shading and cold events during model years 1215–1260 highlighted by the blue shading) and others limited to approximately 1 yr (e.g., model years 360–390). There is also considerable range in the maximum amplitude of simulated ENSO events, with the strongest events exceeding 3°C and the moderate events attaining values ~1.5°C. The variety of ENSO behavior in the model is qualitatively similar to that in nature, at least as sampled by the short observational record (Fig. 2, upper left).

Overall, the CCSM4-1° control integration overestimates the amplitude of Niño-3.4 SST variability compared to observations, with a standard deviation of 1.06°C for the full 1300-yr model record compared to 0.75°C for the detrended HadISST data during 1900–2011. To quantitatively assess the low-frequency changes in ENSO amplitude discussed above, we computed the standard deviation of the Niño-3.4 index ($\delta_{\text{Niño-3.4}}$) for running 30-yr periods from observations and the model (Figs. 3a,b, respectively). Consistent with one’s visual impression from Fig. 2, the HadISST $\delta_{\text{Niño-3.4}}$ exhibits a secular increase during the twentieth century, from a minimum of 0.6°C during 1920–50 to a maximum of

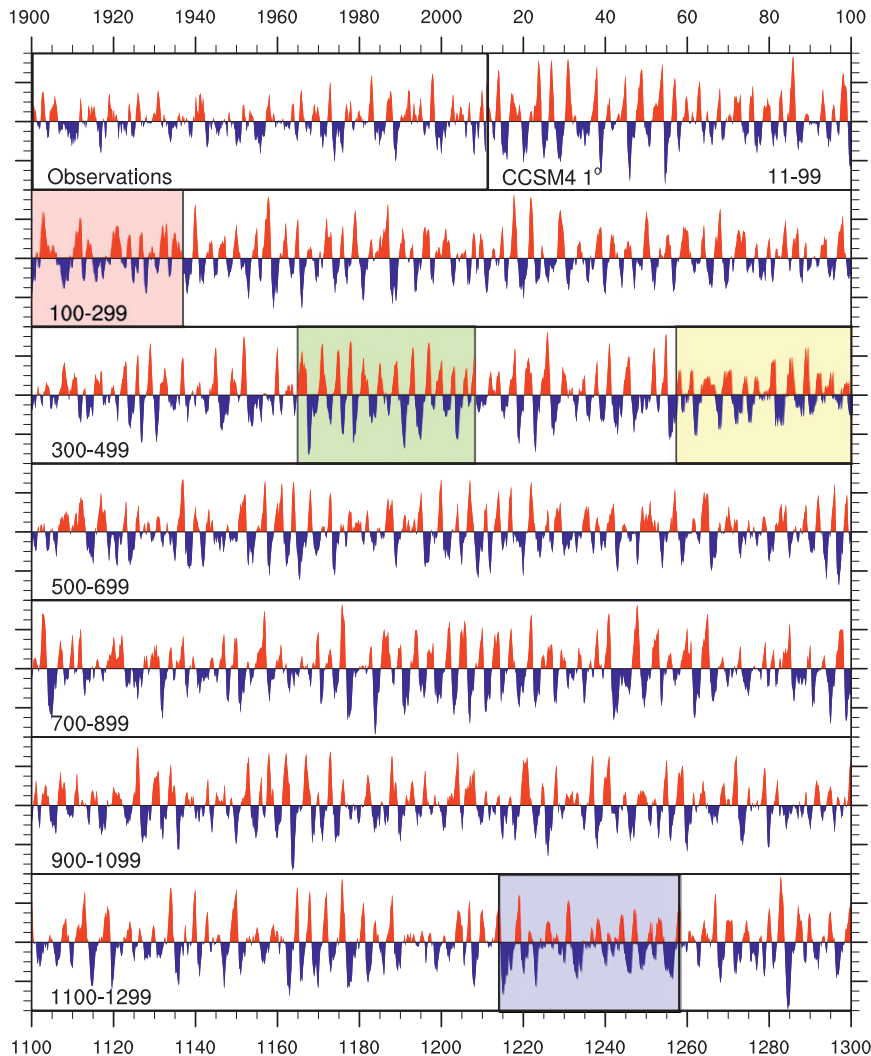


FIG. 2. The Niño-3.4 SST index from (top left) detrended HadISST observations during 1900–2011, and (remaining panels) the 1300-yr CCSM4-1° preindustrial control integration. (top right) Model years 11–99 are shown in the first row on right side, and the remaining rows show each subsequent 200-yr period as marked. Shaded boxes are discussed in the text. Tick marks on the y axis are every 0.5°C.

0.95°C during 1970–2000. While some of the increase may result from external forcing and inhomogeneities in the data record, paleoclimate records suggest a similar range of natural variability (Li et al. 2011). These observed low-frequency changes in ENSO amplitude provide a benchmark for assessing the range of ENSO modulation due to natural variability in the model. The 1300-yr CCSM4-1° control integration exhibits a two-fold range (0.7°–1.4°C) in $\bar{\sigma}_{\text{Niño-3.4}}$ for running 30-yr periods (Fig. 3b). Thus, the model exhibits 30-yr periods in which $\bar{\sigma}_{\text{Niño-3.4}}$ falls within the upper range of the HadISST observations but never below the long-term mean HadISST value.

Power spectrum analysis of the Niño-3.4 SST index is shown in Fig. 4 for a 300-yr segment of the CCSM3-T85

control integration, the full 1300-yr CCSM4-1° control integration, and the HadISST observations. The observational results are shown for two periods, 1900–2010 and 1950–2010, to give an indication of the sensitivity of the spectra to different record lengths [similar results are found for the extended reconstructed sea surface temperature, version 3 (ERSSTv3); not shown]. The CCSM4-1° Niño-3.4 record exhibits a single sharp spectral peak in the 3–6-yr band, while observations show a double-peak structure spanning the period range 3.5–8 yr. The maximum power is approximately twice as large in the model compared to HadISST (note that to quantitatively compare the variance between the model and observations, the curves must be integrated over the frequency

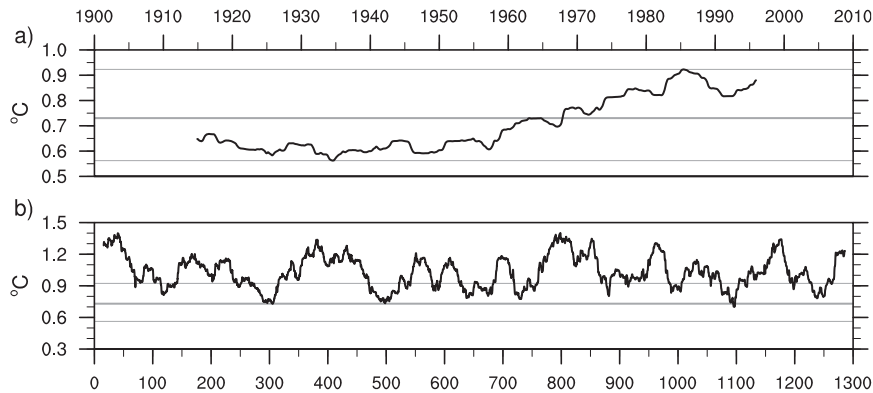


FIG. 3. Standard deviations ($^{\circ}\text{C}$) of the Niño-3.4 SST index for running 30-yr periods: (a) detrended observations (HadISST, 1900–2010); and (b) CCSM4-1 $^{\circ}$ 1300-yr control integration. The thin (thick) horizontal lines in both panels delineate the minimum and maximum (mean) values from HadISST.

band of interest). CCSM3-T85 exhibits better agreement with HadISST in terms of maximum power, but the dominant period is too short (1.75–3 yr). The period of ENSO in CCSM4-2 $^{\circ}$ is similar to that in CCSM4-1 $^{\circ}$ but the power is considerably greater (not shown).

A well-known characteristic of observed ENSO events is the tendency for phase locking to the seasonal cycle, with warm and cold events peaking near the end of the calendar year. Indeed, the standard deviation of the observed Niño-3.4 SST index maximizes (1.1°C) in December and reaches a minimum (0.55°C) in April (Fig. 5). The seasonal cycle based on CCSM4-1 $^{\circ}$ lags the observations by 1–2 months, with a maximum (1.35°C) in January and a minimum (0.75°C) in May (Fig. 5). The timing of the seasonal cycle is similar in CCSM4-2 $^{\circ}$ as in CCSM4-1 $^{\circ}$, but the values are $\sim 0.2^{\circ}\text{C}$ larger (and $\sim 0.5^{\circ}\text{C}$ greater than observations). CCSM3-T85 exhibits realistic timing of the seasonal cycle, but the range is weaker and there is an erroneous secondary maximum during June–July (Fig. 5).

We assess the regularity of ENSO in observations and CCSM4-1 $^{\circ}$ and CCSM3-T85 using the autocorrelation of the Niño-3.4 record as a simple metric. The monthly lead-lag correlations are computed with respect to the December time series (denoted Dec 0 in Fig. 6). The autocorrelation curve for CCSM4-1 $^{\circ}$ is qualitatively similar to observations, with strongest negative values at approximately ± 2 yr consistent with the realistic 3–6-yr ENSO period. However, the maximum negative autocorrelations are overestimated (~ -0.45 compared to -0.25), indicative of greater ENSO regularity in the model compared to nature. CCSM3-T85 displays an even higher degree of ENSO regularity than CCSM4-1 $^{\circ}$ (maximum negative autocorrelations ~ -0.65), and these occur at shorter lags (Dec $^{-1}$ and Dec $^{+1}$) reflecting

the biennial periodicity. The increased irregularity of ENSO in CCSM4-1 $^{\circ}$ compared to CCSM3-T85 constitutes a notable improvement.

2) COMPOSITE EL NIÑO AND LA NIÑA EVENTS

Following Okumura and Deser (2010), we construct a composite El Niño (La Niña) event by selecting years

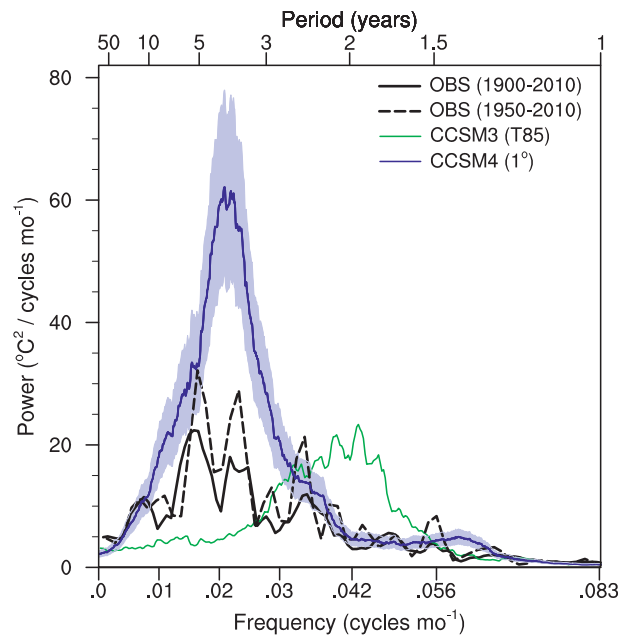


FIG. 4. Power spectrum [$^{\circ}\text{C}^2$ (cycles month) $^{-1}$] of the Niño-3.4 SST index from detrended observations (HadISST, dashed black curve for 1900–2010 and solid black curve for 1950–2010), CCSM4-1 $^{\circ}$ (model years 1–1300; blue curve), and CCSM3-T85 (model years 100–599; green curve). The light-blue shading depicts the confidence intervals for the CCSM4-1 $^{\circ}$ spectrum based on the individual spectra for each 100-yr segment.

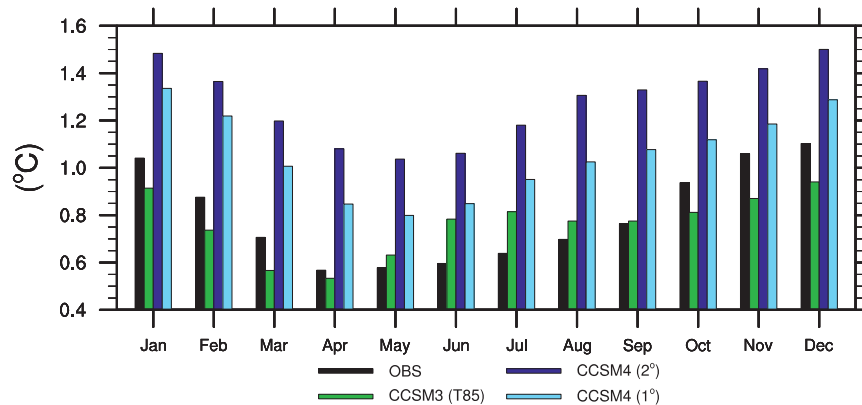


FIG. 5. Monthly standard deviation ($^{\circ}\text{C}$) of the Niño-3.4 SST index for detrended observations (HadISST, 1900–2010), CCSM4-1 $^{\circ}$, CCSM4-2 $^{\circ}$, and CCSM3-T85 as indicated.

when the December Niño-3.4 SST Index exceeds 1 (is less than -1) standard deviation (δ). To reduce month-to-month noise, the Niño-3.4 record is smoothed with a 3-month binomial filter before selecting the events. With these criteria, the observed composites for the period 1900–2010 (1957–2008) contain 19 (7) El Niño (EN) events and 14 (7) La Niña (LN) events. The simulated composites are based on 80 (82) EN (LN) events for CCSM4-1 $^{\circ}$ and 53 (46) EN (LN) events for CCSM3-T85. To facilitate comparison of spatial patterns between the models and observations, we have scaled the model composite fields by the value of the December

Niño-3.4 Index in the observed EN (LN) composite divided by that in the simulated EN (LN) composite. These scaling factors are: 0.75 (0.85) for EN (LN) in CCSM4-1 $^{\circ}$ and 1.26 (1.18) for EN (LN) in CCSM3-T85 when comparing to observations during 1900–2010; and 0.61 (0.76) for EN (LN) in CCSM4-1 $^{\circ}$ and 1.03 (1.06) for EN (LN) in CCSM3-T85 when comparing to observations during 1957–2008. We denote the year that includes the December value of the Niño-3.4 Index used in the compositing criteria as year 0, and the previous and subsequent years as -1 and $+1$, respectively.

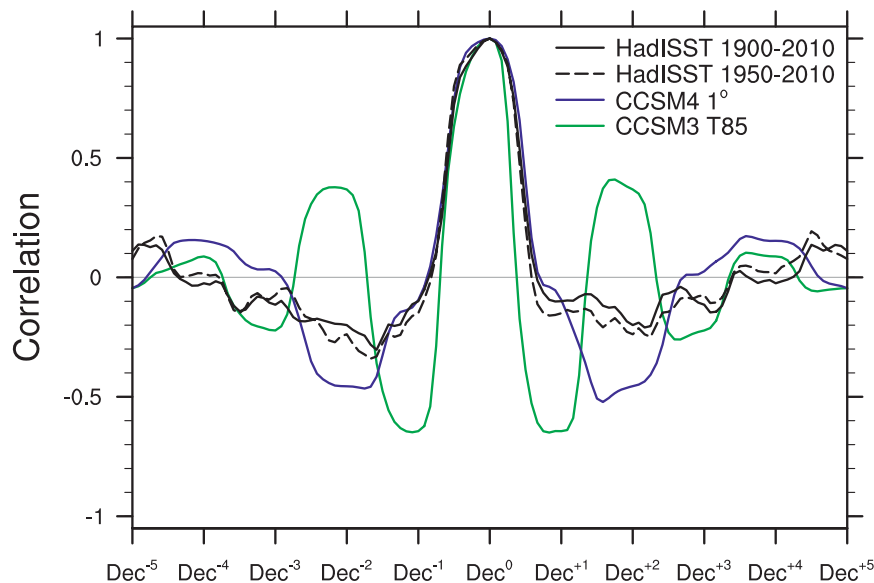


FIG. 6. Monthly autocorrelation curves of the Niño-3.4 SST index from observations (detrended HadISST, solid black curve for 1900–2010 and dashed black curve for 1950–2010), CCSM4-1 $^{\circ}$ (model years 1–1300; blue curve), and CCSM3-T85 (model years 100–599; green curve). Autocorrelations are computed from the December Niño-3.4 index (Dec^0) and span the previous and subsequent 5 yr. The indices were smoothed with a 3-point binomial filter before computing the autocorrelations.

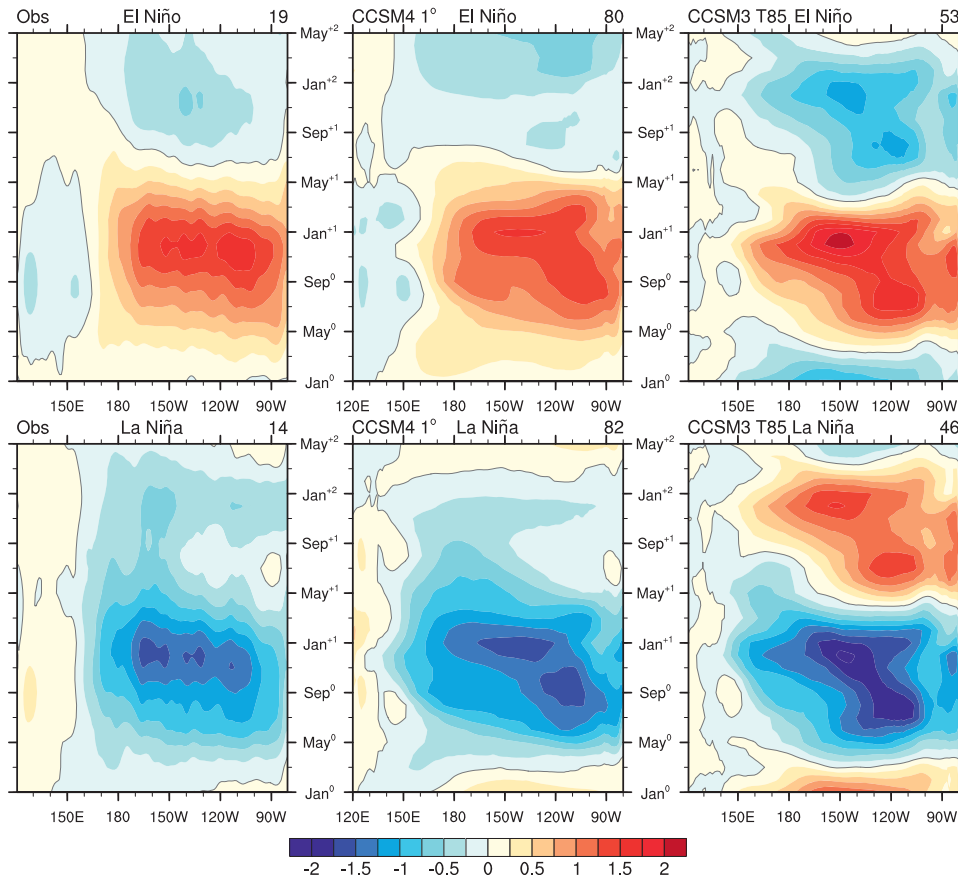


FIG. 7. Longitude–time sections of composite SST anomalies along the equator (3°N – 3°S) for (top) El Niño and (bottom) La Niña based on (left) observations (detrended HadISST 1900–2010), (middle) CCSM4– 1° (model years 1–1300), and (right) CCSM3–T85 (model years 100–599). The model composites have been scaled to match the observed composite amplitude of the Niño-3.4 SST index in Dec⁰. The number at the top right of each panel indicates the number of events used for the composite.

Time–longitude plots of SST anomalies along the equator for the composite EN and LN events are shown in Fig. 7. Similar to observations (Ohba and Ueda 2009; Okumura and Deser 2010), CCSM4– 1° exhibits clear asymmetries between the warm and cold phases of ENSO. The most striking asymmetry is the extended duration of LN through Feb⁺², more than a year following the peak of the event in Dec⁰, compared to EN which transitions to a weak LN event starting in Jun⁺¹. Another notable difference is that the eastern equatorial Pacific SST anomalies extend approximately 20° – 30° of longitude farther west during LN compared to EN. In contrast, warm and cold events are nearly mirror images of one another in CCSM3–T85: both last approximately 12 months and transition to the opposite sign in the following year. There is a modest ($\sim 10^{\circ}$ of longitude) westward expansion of the SST anomalies during LN compared to EN in CCSM3–T85. Both models exhibit westward SST anomaly propagation from approximately

90° to 150°W during the second half of year 0. Westward propagation is less evident in the observations; however, composites based on the first half of the twentieth century display stronger westward propagation (not shown, but see Fig. 3 in Okumura and Deser 2010).

The asymmetry in duration between EN and LN is confirmed by the frequency distributions of individual events (Fig. 8). EN (LN) event duration is defined as the number of consecutive months for which the Niño-3.4 SST index exceeds 0.25 standard deviations (is less than -0.25 standard deviations) after Dec⁰, using the criteria above for event selection. The results show that $\sim 80\%$ ($\sim 70\%$) of observed EN (LN) events last less than (more than) 8 months after Dec⁰. CCSM4– 1° exhibits a similar, albeit less pronounced, shift in the frequency distribution of event duration: $\sim 70\%$ ($\sim 60\%$) of EN (LN) events last less (more than) 8 months after Dec⁰. In the model, LN event duration exhibits a double peak in the frequency distribution, with approximately equal

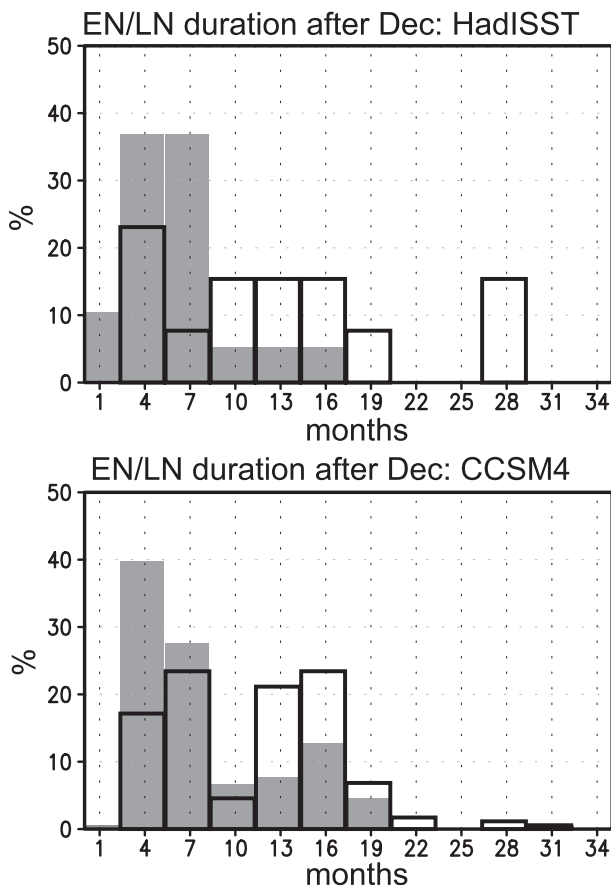


FIG. 8. Frequency distribution (%) of El Niño (shaded bars) and La Niña (black outline bars) duration (in months) after the December peak for (top) observations (detrended HadISST 1900–2010) and (bottom) CCSM4-1° (model years 1–1300). The number of EN (LN) events in each 3-month bin has been divided by the total number of EN (LN) events.

numbers of events in the 4–7-month and 13–16-month duration range.

A more complete view of the composite seasonal evolution of ocean-atmosphere anomalies during EN (LN) is given in Fig. 9 (Fig. 10) for observations and CCSM4-1°. The composites span nearly two full years, beginning in March–May⁰ (MAM⁰) at the event onset, and ending in December–February⁺² (DJF⁺²) a full year after the event peak. The left-hand panels show SST and precipitation, and the right-hand panels show the depth of the 15°C isotherm (Z15; a proxy for thermocline depth) and surface wind vectors. The seasonal evolution of the composite EN is similar between the model and observations (Figs. 9a,b). Both show the growth of positive SST and precipitation anomalies over the equatorial eastern Pacific beginning in MAM⁰ and peaking in DJF⁺¹. Negative SST and precipitation anomalies develop over the western Pacific and eastern Indian

Ocean during June–August⁰ (JJA⁰) through DJF⁺¹. The Indian Ocean dipole (IOD; see Schott et al. 2009 for a review), characterized by positive (negative) SST anomalies in the western (eastern) Indian Ocean, is present in September–November⁰ (SON⁰), and in the model also extends into DJF⁺¹. The warm event weakens substantially in MAM⁺¹ and transitions to a cold event starting in JJA⁺¹ with subsequent growth through DJF⁺². The demise of EN and transition to LN occur a couple of months later in the model compared to nature.

SST anomaly growth during EN is accompanied by a deeper thermocline in the eastern Pacific and a shallower thermocline in the western Pacific, consistent with the westerly surface wind anomalies over the central and western Pacific. As the event decays, the negative Z15 anomalies expand eastward along the equator, such that by JJA⁺¹ when the SST anomalies transition to a LN, the thermocline is anomalously shallow across the entire equatorial Pacific. While the growth phase of LN is similar to that of EN but with opposite sign, the decay phase follows a different evolution (Figs. 10a,b). Most notable is the extended duration of LN (negative SST anomalies, below normal precipitation, easterly wind anomalies, enhanced thermocline tilt) through DJF⁺².

3) MECHANISTIC ANALYSIS OF THERMOCLINE VARIABILITY

Here, we provide a more mechanistic analysis of ENSO thermocline depth variations within the framework of the delayed oscillator and recharge oscillator paradigms. We note that such an analysis emphasizes the linear aspects of EN and LN and does not take into account the asymmetric features of warm and cold events documented above. The leading modes of thermocline variability in CCSM4-1°, defined through EOF analysis of Z15 anomalies (Figs. 11d,e), are very similar to those computed from the SODA ocean reanalysis (Figs. 11a,b), as well as those obtained from observations (Meinen and McPhaden 2000). The first EOF is characterized by an east–west dipole, indicative of changes in the zonal thermocline slope, while the second EOF describes a deepening or shoaling of the equatorial thermocline as a whole. Qualitatively similar patterns were found in a subset of the Climate Model Intercomparison Project version 3 (CMIP3) models (Capotondi et al. 2006), although pattern details varied from model to model. The two leading EOFs of thermocline depth variability in CCSM3-T85 are also shown in Fig. 11, based on the period 1870–1999 from a twentieth-century integration; however, similar results are obtained with the CCSM3-T85 control integration (not shown, but see Deser et al. 2006). The main difference between the EOF patterns in CCSM3-T85 and CCSM4-1° is the meridional scale of the equatorial

El Niño (Observations 1958-2007)

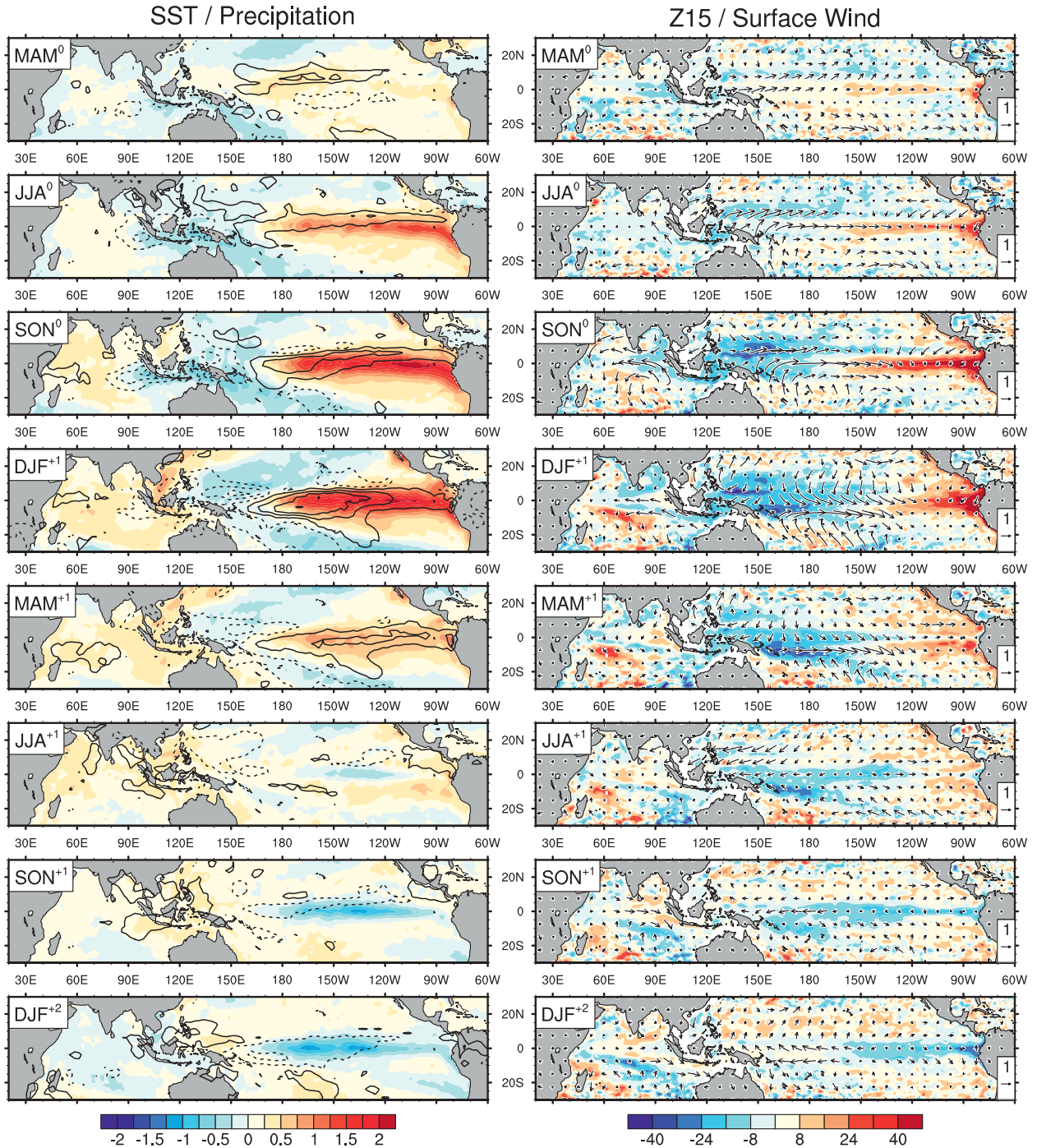


FIG. 9. (a) Observed El Niño seasonal composite evolution starting in MAM⁰ and ending in DJF⁺² for (left) SST and precipitation anomalies and (right) thermocline depth (Z15) and surface wind anomalies. SST (°C) and Z15 (m) are shaded; precipitation contours (solid for positive anomalies, dashed for negative anomalies) are ± 9 , ± 7 , ± 5 , ± 3 , ± 1 mm day⁻¹; and the wind vector scale (m s⁻¹) is shown at the bottom right of each panel. Results are based on the period 1958–2007 except for precipitation, which is for 1979–2007.

anomalies. In CCSM3–T85, the equatorial thermocline variations are confined to the latitude band 10°S–5°N, with anomalies of opposite sign to the north and south;

whereas in CCSM4–1° they are broader in meridional extent especially in the Southern Hemisphere, in better agreement with the SODA reanalysis.

El Niño (CCSM4 1° 800-1299)

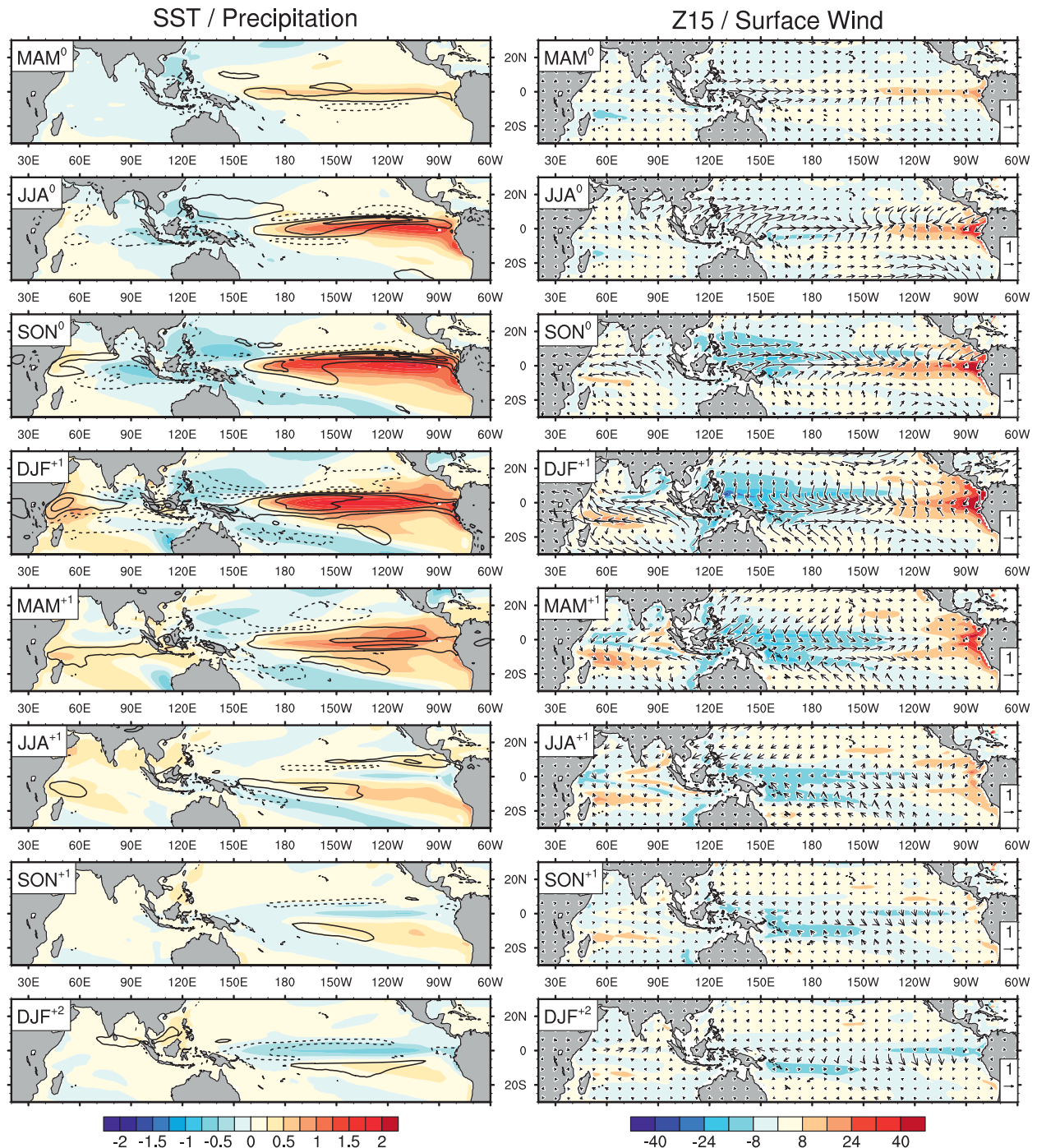


FIG. 9. (b) As in (a), but for CCSM4-1° using model years 800–1299. All of the model composite fields have been scaled such that the simulated composite amplitude of the Niño-3.4 SST index in Dec⁰ matches observations.

The leading patterns of thermocline variability displayed in Fig. 11 have been interpreted as consistent with the recharge oscillator paradigm for ENSO (Jin 1997a,b; Meinen and McPhaden 2000; Capotondi

et al. 2006). That is, the mature phase of a warm event is characterized by a deeper thermocline in the eastern Pacific and a shallower thermocline in the western Pacific (positive phase of EOF1). The anomalous zonal slope of

La Niña (Observations 1958-2007)

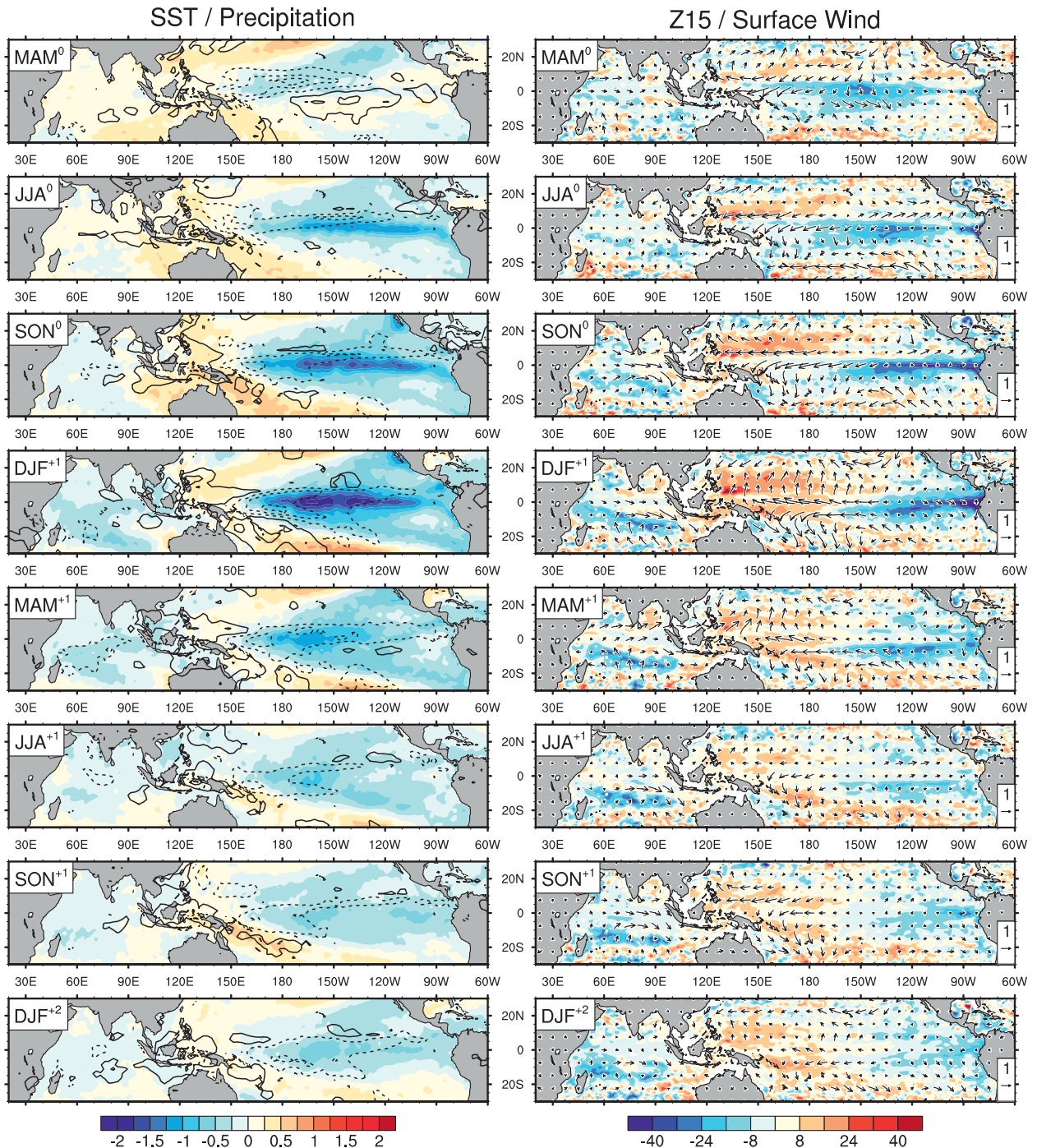


FIG. 10. (a) As in Fig. 9a, but for La Niña.

the thermocline is associated with an anomalous poleward Sverdrup transport responsible for discharging warm water from the equatorial thermocline, resulting in a shallower-than-average thermocline across the equatorial Pacific (positive phase of EOF2). Upwelling of

colder water in the eastern Pacific subsequently erodes the original warm SST anomaly and leads to the opposite phase of the cycle. In this view, the two leading EOFs are expected to be approximately in quadrature. Indeed, lag-correlation analysis between the two principal component

La Niña (CCSM4 1° 800-1299)

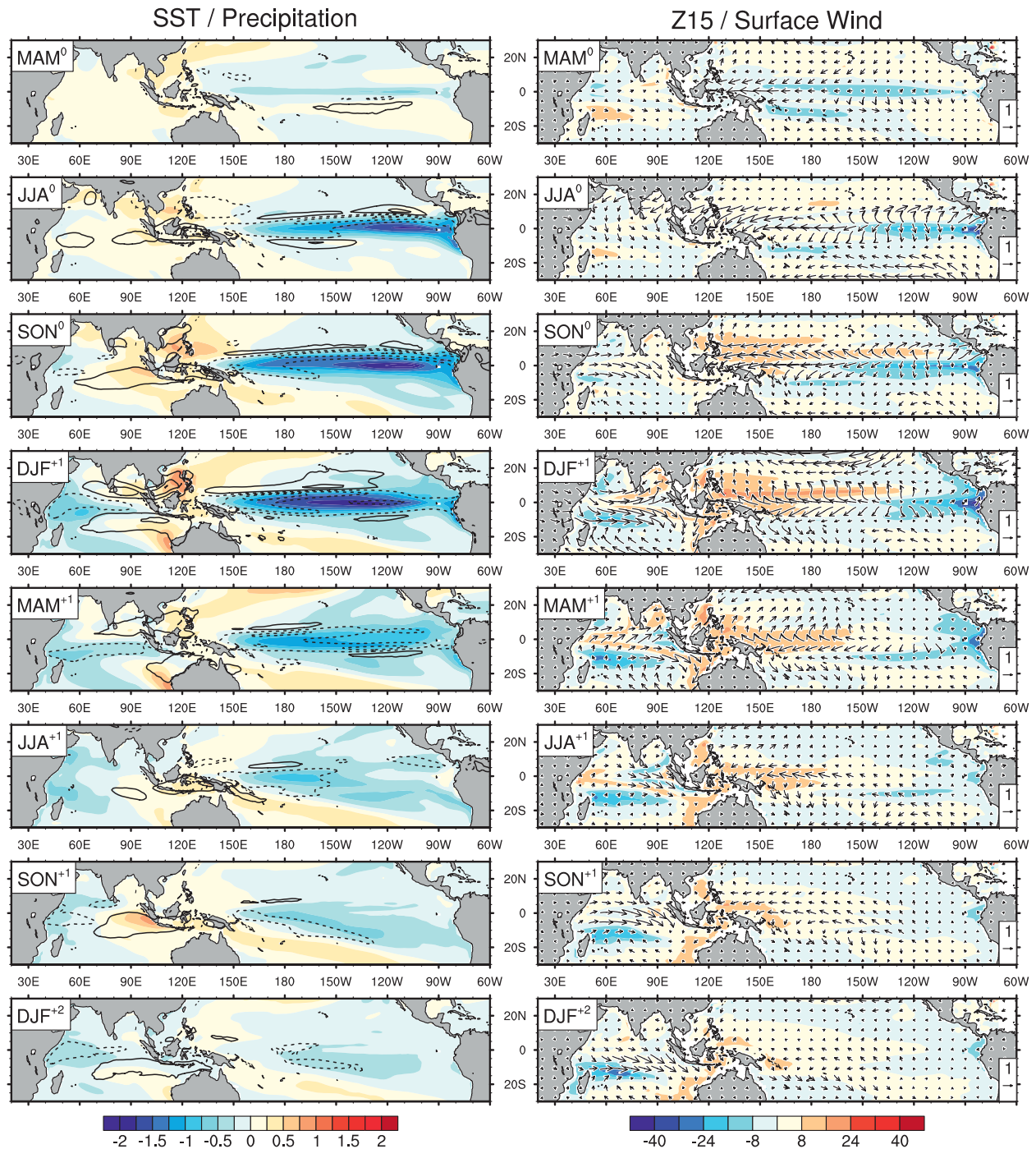


FIG. 10. (b) As in Fig. 9b, but for La Niña.

(PC) time series confirms that PC1 (corresponding to the peak of a warm event) leads PC2 (discharged thermocline) by ~ 10 months in SODA and CCSM4-1°, and by 7 months in CCSM3-T85, with maximum correlations of 0.59 in SODA, 0.79 in CCSM4, and 0.76 in CCSM3

(Fig. 11, right-hand panels). The difference in lag of the maximum correlation between the two models reflects their different ENSO periods. The approximate 10-month lag in both SODA and CCSM4-1° is in good agreement with the value of ~ 9 months estimated

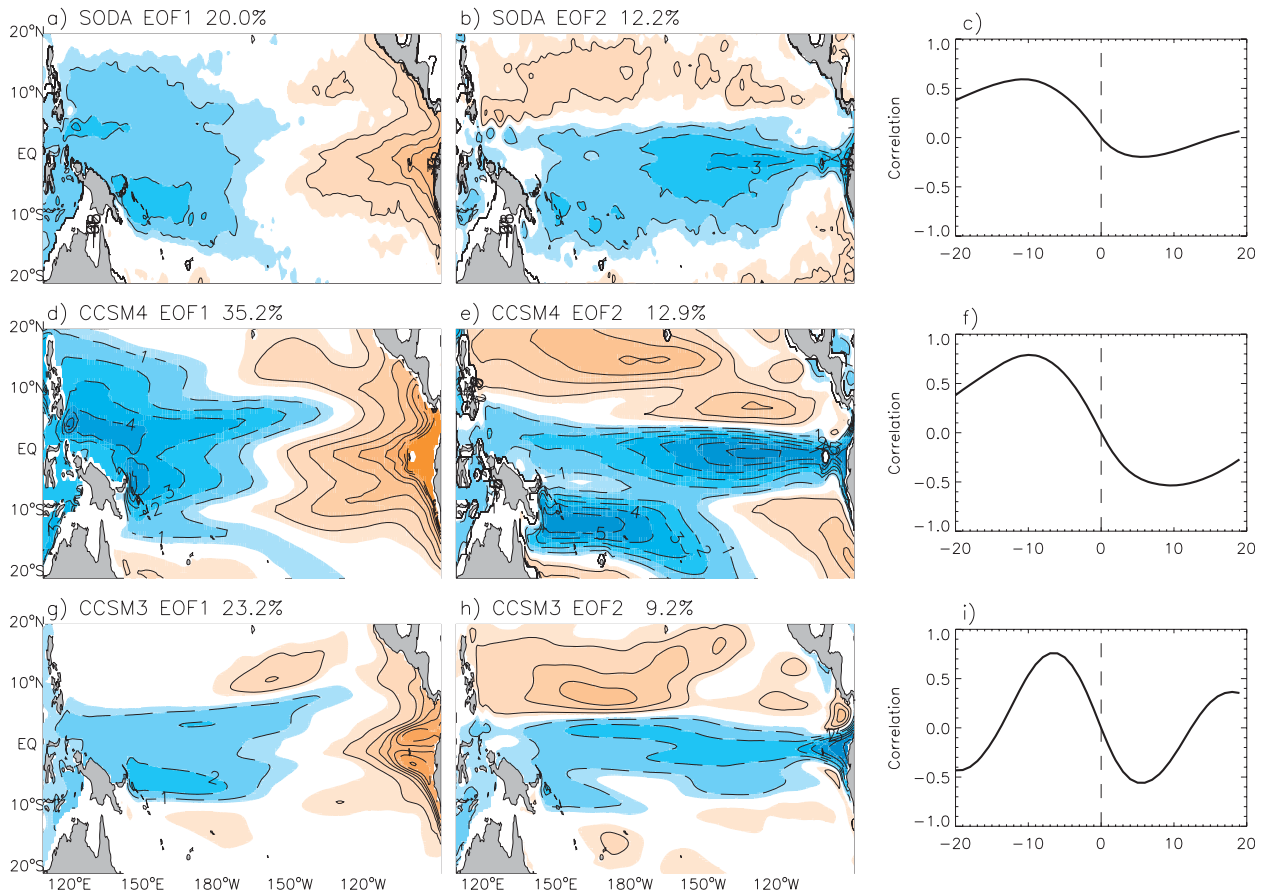


FIG. 11. (left),(middle) The two leading EOFs of thermocline depth (Z_{15}) for (top) SODA, (middle) CCSM4-1°, and (bottom) CCSM3-T85. Blue shading is for negative values (thermocline shallower than average), and orange shading is for positive values (thermocline deeper than average). The percent variance explained by each mode is given in the panel title. A 5-month running mean was applied to the SODA data before computing the EOFs. (right) Lag-correlation curves between PC1 and PC2; negative (positive) lags are for PC1 leading (lagging) PC2. The lag of maximum correlation, in absolute value, is approximately a quarter of a cycle. All correlations are based on the total duration of the time series for each product, namely (top to bottom) 51 yr for SODA, 500 yr (model years 800–1300) for CCSM4-1°, and 130 yr (1870–1999) for CCSM3-T85.

from observations during 1980–2000 by Meinen and McPhaden (2000).

The spatial structure of the anomalous wind stress associated with ENSO is considered an important factor in setting the ENSO time scale (Kirtman 1997; An and Wang 2000; Capotondi et al. 2006; Neale et al. 2008). In particular, the meridional scale of the zonal wind stress anomalies associated with ENSO determines the latitudes of largest wind stress curl anomalies responsible for enhanced Rossby wave activity (Capotondi 2008). Because of the decrease of the Rossby wave phase speed with latitude, a meridionally broader structure of anomalous wind stress will result in a longer adjustment time scale of the equatorial thermocline and in a longer ENSO period. Figure 12 compares the structures of the anomalous zonal wind stress regressed upon the normalized Niño-3.4 index in the ERA-40 reanalysis, CCSM4-1°,

and CCSM3-T85. While the anomalous wind stress in CCSM3-T85 is tightly confined within 5° of the equator, CCSM4-1° exhibits zonal wind stress anomalies of considerably broader meridional extent, especially in the Southern Hemisphere where the anomalous winds extend southeastward in better agreement with the regression pattern obtained from the ERA-40 reanalysis (see also Neale et al. 2008). The broader meridional scale for CCSM4-1° can clearly be detected in the right panels of Fig. 12, which shows the zonal average of the zonal wind regression patterns.

Capotondi et al. (2006) showed that the limited meridional extent of the zonal wind stress anomalies was common to many of the CMIP3 models and was associated with an ENSO time scale shorter than observed. Figure 13 shows the ENSO period versus the meridional scale of the zonal wind stress anomalies (denoted L_y) for

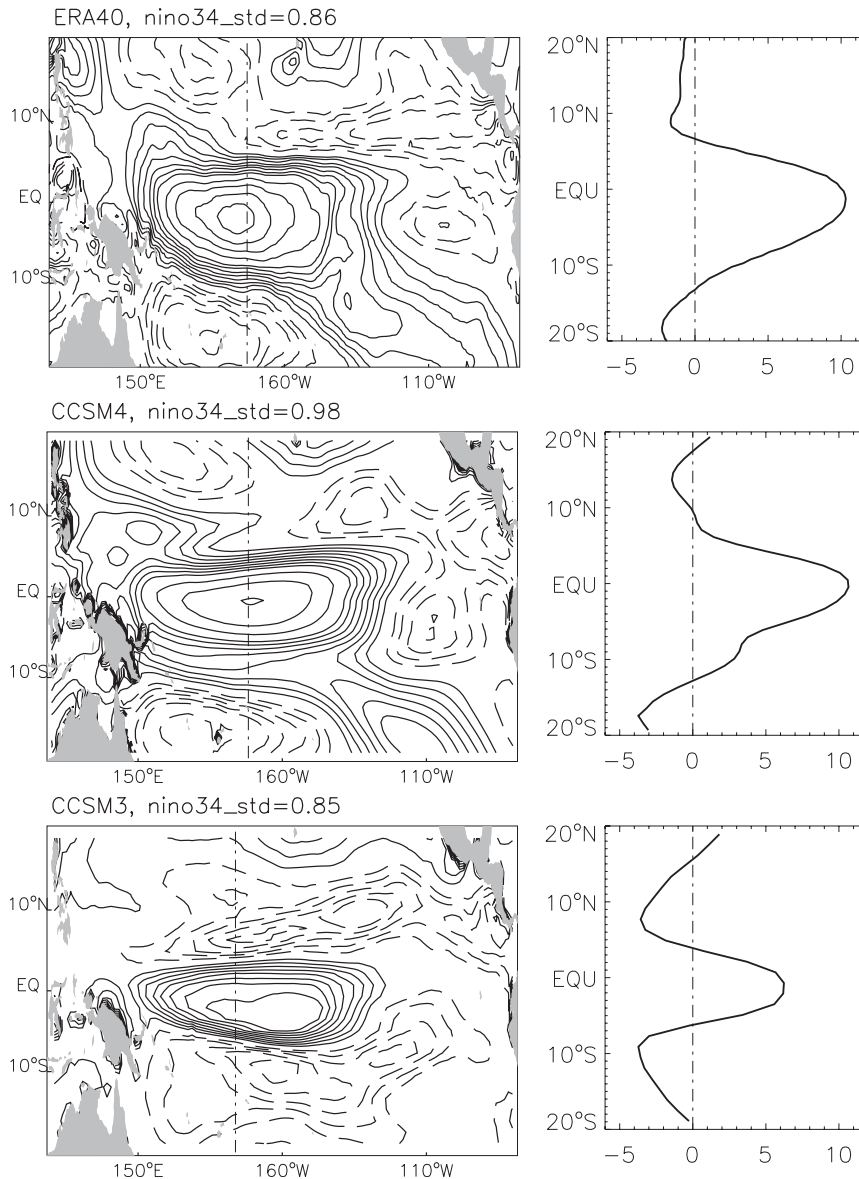


FIG. 12. (left) Regressions of the zonal surface wind stress component upon the normalized Niño-3.4 index for (top) ERA-40, (middle) CCSM4-1°, and (bottom) CCSM3-T85. The contour interval is $1 \times 10^3 \text{ N m}^{-2}$ for values between 1 and 8, and $2 \times 10^3 \text{ N m}^{-2}$ for values larger than 8 in absolute value. (right) Zonal average of the patterns in the left panels. The latitudes of zero crossing are used to define the meridional scale of the wind stress anomalies (L_y).

the subset of CMIP3 models analyzed by Capotondi et al. (2006; filled circles), the GFDL Climate Model version 2.1 (CM2.1) (diamond), the CCSM4-1° (star), and two observational estimates (open circle) uses L_y from the NCEP-NCAR reanalysis and ENSO period from the Instituto Nazionale di Geofisica e Vulcanologia (INGV) ocean analysis, which is forced by NCEP as described in Capotondi et al. (2006). The other (triangle) uses L_y from the ERA-40 reanalysis and ENSO period from the SODA ocean analysis, which

is forced by ERA-40. Characteristics of the GFDL CM2.1 ENSO simulation have been reported in many studies including Wittenberg (2009). In all products, the period was estimated from the frequency corresponding to the maximum spectral power as in Capotondi et al. (2006). The meridional scale was estimated for each model using the distance between the zero crossing points of the zonal average of the regression patterns. The meridional scales for the CMIP3 models considered by Capotondi et al. (2006) range between 10° and 16° , smaller than the

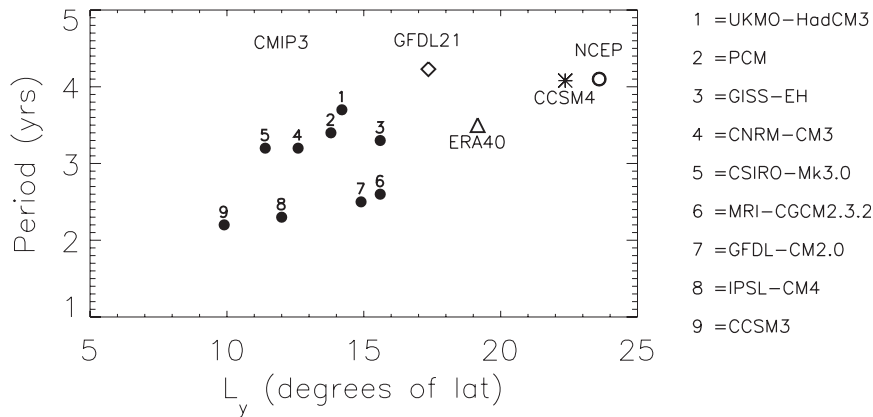


FIG. 13. ENSO period (determined from the frequency of maximum spectral power of the Niño-3.4 index) vs the meridional width of the zonal wind stress anomalies (L_y) for the nine CMIP3 models used in Capotondi et al. (2006; filled circles identified by number), GFDL CM2.1 (diamond), CCSM4-1° (star), ERA-40/SODA (triangle), and NCEP reanalysis-INGV (open circle). Note that CCSM4-1° lies within the range of the observational estimates.

19°–24° range spanned by the two atmospheric reanalyses. In contrast, L_y for CCSM4-1° is ~22°, well within the range of the observational estimates. The GFDL CM2.1 has an $L_y \sim 17^\circ$, intermediate between observations and the CMIP3 subset. Collectively, the models and observations exhibit an approximate linear relationship between L_y and ENSO period.

4) GLOBAL TELECONNECTIONS

The tropical precipitation changes during ENSO initiate global atmospheric circulation anomalies that in turn affect the surface climate. Here we compare observed and simulated ENSO teleconnections for the peak seasons JJA⁰, SON⁰, DJF¹, and MAM¹. Because of the largely symmetric nature of the global atmospheric teleconnections during EN and LN in these seasons (not shown), we summarize the results in terms of composite difference maps (EN minus LN). SLP and surface temperature (300-hPa streamfunction and precipitation) anomalies are shown in the left (right) panels for the NCEP-NCAR reanalyses (Fig. 14) and CCSM4-1° (Fig. 15). The model composites have been scaled to match the observed composite amplitude of the Niño-3.4 SST index in Dec⁰.

In JJA⁰ when ENSO is underway, the main SLP response occurs over the South Pacific where it takes the form of a meridional dipole, with positive anomalies near Antarctica and negative anomalies to the north, stretching from New Zealand to South America. The pattern and amplitude of the SH response is well simulated by the model. This teleconnection pattern persists during SON⁰ as ENSO continues to intensify; however, the amplitude is somewhat underestimated by the model. In DJF¹, the strongest SLP response occurs in the Northern Hemisphere, with negative anomalies over

the North Pacific and a weaker meridional dipole over the North Atlantic. The model's teleconnection to the North Pacific in this season is more zonally oriented and spatially extensive than observed. The model erroneously persists the anomalous deepening of the Aleutian low pressure system into MAM¹, similar to that documented for the Hadley Centre Atmospheric Model version 3 (HadAM3) by Spencer and Slingo (2003). Overall, the SLP response over the Southern Hemisphere exhibits less seasonal dependence than that over the Northern Hemisphere, consistent with Jin and Kirtman (2009) among others.

The tropical upper-level streamfunction anomalies display a classical response to heating, with anticyclonic centers on the northern and southern flanks of the equatorial Pacific precipitation anomalies. Upper-level wave trains emanate from the tropical heat source, with largest amplitudes generally in the winter and spring hemispheres. Less seasonality is evident in the Southern Hemisphere compared to the Northern Hemisphere, consistent with Jin and Kirtman (2009). The simulated wave train response over the North and South Pacific tends to be more zonally elongated than in observations, similar to the character of the extratropical SLP response. The model lacks a well-defined wave train response over the North Pacific in SON⁰.

The precipitation response is generally well simulated in CCSM4-1°. In the tropical Pacific, the ITCZ and SPCZ shift equatorward, inducing positive precipitation anomalies across the equatorial Pacific and negative anomalies along the poleward flanks of the convergence zones. Reduced precipitation occurs over the Maritime Continent, the eastern tropical Indian Ocean, the tropical Atlantic Ocean, and Brazil, while enhanced rainfall is found over the western portion of the Indian Ocean

(except in JJA⁰). The model produces erroneous positive precipitation anomalies over the equatorial portion of the Maritime Continent and eastern Indian Ocean in DJF⁺¹ and MAM⁺¹. The simulated rainfall anomalies are also too narrowly confined near the equator and too weak over the SPCZ.

The model captures the main features of the observed terrestrial air temperature response, including the negative (positive) temperature anomalies over eastern Russia and the southeastern United States (western Canada and Alaska) in SON⁰, DJF¹, and MAM¹. However, the amplitude of the temperature response over Alaska and western Canada in MAM¹ (and to a lesser extent DJF¹) is greatly exaggerated, likely as a result of the erroneous deepening of the Aleutian low SLP response. Similarly, the model's erroneous positive SLP response over northern Eurasia may be responsible for the incorrect sign of the underlying temperature response. In polar regions, the simulated surface temperature response reflects changes in sea ice concentration, with positive temperature anomalies indicative of negative sea ice anomalies and vice versa. The largest sea ice changes occur near Antarctica where reduced (increased) ice cover is associated with anomalous northerly (southerly) winds and warm (cold) air advection as inferred from the SLP response. Similar responses are found in observations (not shown, but see Yuan 2004).

5) EXTRATROPICAL UPPER-OCEAN THERMAL RESPONSE

The ENSO composites in Figs. 14 and 15 indicate that the extratropical SST anomaly patterns and amplitudes are generally well simulated in CCSM4-1°. In particular, negative SST anomalies extend eastward and poleward across the North and South Pacific from SON⁰ through MAM⁺¹, with amplitudes of 0.5°–1.5°C. The vertical structure and temporal evolution of upper-ocean thermal anomalies in the central North Pacific (23°–40°N, 162°E–140°W) and South Pacific (23°–40°S, 160°–93°W) are shown in Fig. 16 for composite EN and LN events from SODA and CCSM4-1° (regions are marked on the MAM⁺¹ panel in Figs. 14 and 15). The central North Pacific region (Fig. 16a) shows clear asymmetries between EN and LN in both SODA and the model. During EN, negative temperature anomalies are formed during winter and extend through the deep mixed layer (~140 m in the model and ~110 m in SODA). These anomalies persist at depth beneath the mixed layer into the subsequent spring, summer, and fall, penetrating slowly downward with time. Weak positive temperature anomalies replace the negative anomalies in the following winter, consistent with the transition of EN to LN (recall Figs. 7 and 9). The mixed layer deepens by 20–30 m in February–March of year +1 compared to the following

winter in both the model and SODA. During LN, positive temperature anomalies form during January–March of year +1 and persist beneath the mixed layer during the subsequent spring, summer, and fall. However, the positive anomalies are noticeably shallower than their cold counterparts during EN, consistent with the shallower winter mixed layer. As a result, there is less downward penetration of the positive anomalies with time compared to the EN composite. In January–February of year +2, the sequestered anomalies at depth become re-entrained into the deepened winter mixed layer in both observations and the model. The effectiveness of the re-entrainment results from the extended duration of LN compared to EN. During EN, the change in sign of the surface forcing associated with the transition to LN in the second winter competes with the re-entrainment of subsurface temperature anomalies into the mixed layer. The deepening (shoaling) of the winter mixed layer in year +1 during EN (LN) is due to changes in stability associated with negative (positive) buoyancy and mechanical forcing via changes in wind stress and surface heat fluxes (not shown).

The South Pacific region exhibits a somewhat different seasonal evolution compared to the North Pacific, with the largest thermal anomalies occurring within the shallow summer mixed layer during both EN and LN (Fig. 16b: note that the time axis begins in May⁰ for the South Pacific compared to Oct⁰ for the North Pacific). The anomalies remain largely confined to the mixed layer as it deepens during fall and early winter, exhibiting little downward penetration into the main thermocline and no signal of reemergence.

6) EXTRATROPICAL AND TROPICAL PRECURSORS FOR ENSO

As a first step in identifying ENSO precursors, including the SFM, we examine the EN minus LN composite SLP and SST anomaly fields in the winter (DJF⁰) and spring (MAM⁰) prior to the event peak using the usual compositing criteria (Fig. 17). The SLP anomalies in DJF⁰ exhibit a meridional dipole with centers at 30° and 60°N near 160°W, which is nearly identical to the North Pacific oscillation (NPO), the second leading pattern of interannual SLP variability over the North Pacific in winter (Walker and Bliss 1932; Rogers 1981; Linkin and Nigam 2008). The NPO has been identified as the main pattern of atmospheric variability that initiates the SFM (e.g., Vimont et al. 2003b). When anomalous low pressure occupies the southern lobe of the NPO, the anomalous winds are from the west opposing the trade winds over the central and eastern subtropical Pacific, reducing the wind speed and upward latent flux (not shown), thereby warming the underlying ocean through winter and into spring (Fig. 17). The positive SST anomalies that extend

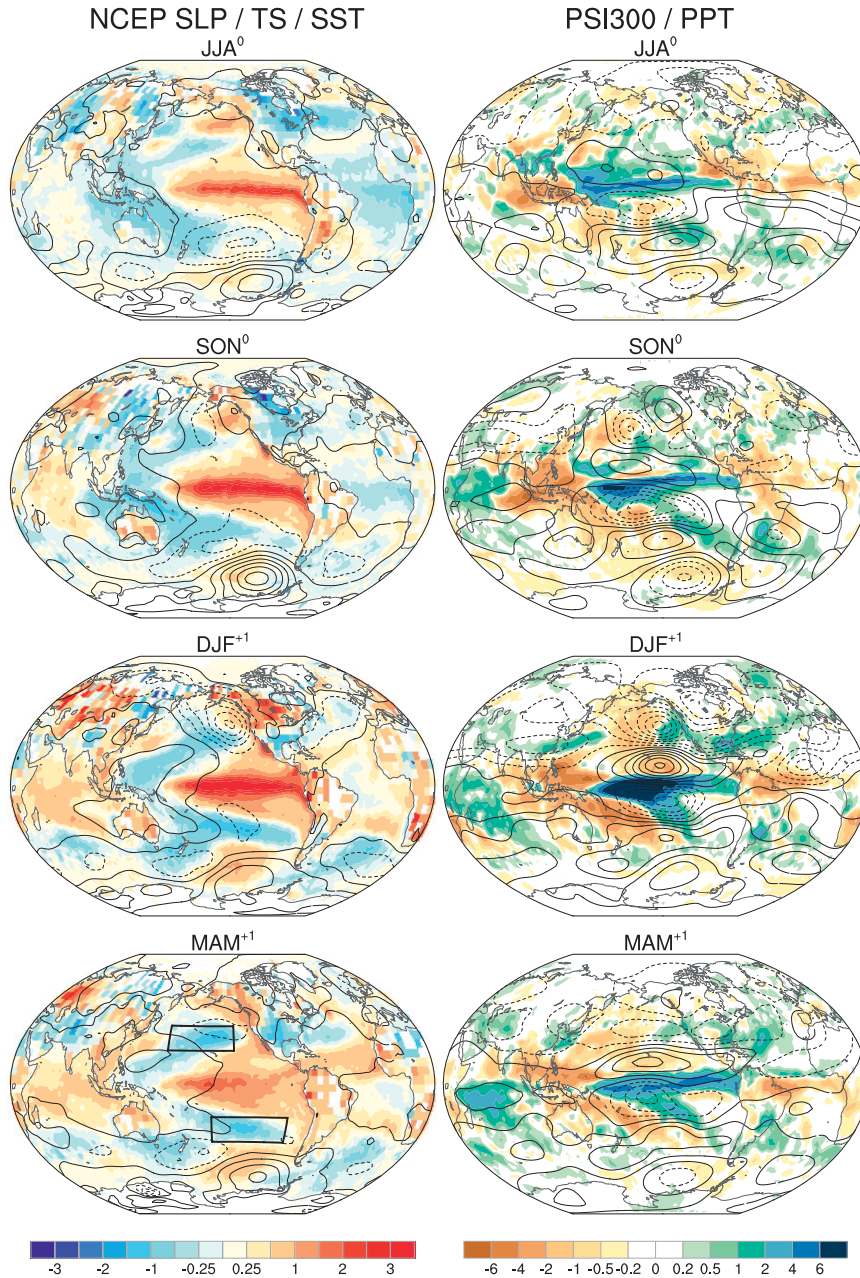


FIG. 14. Observed El Niño minus La Niña composite evolution of (left) SST and terrestrial air temperature ($^{\circ}\text{C}$; shaded) and SLP (contour interval of 2 hPa) and (right) precipitation (mm day^{-1} ; shaded) and 300-hPa streamfunction (contour interval of $3 \times 10^6 \text{ m}^2 \text{ s}^{-1}$) anomalies for (top to bottom) JJA⁰, SON⁰, DJF⁺¹, and MAM⁺¹ based on observations for the period 1958–2007 except for precipitation, which is for 1979–2007. The boxes in the MAM+1 panel outline the regions used for Fig. 16.

into the equatorial Pacific starting in boreal spring (MAM⁰) are enhanced in summer and subsequently develop into a warm event in both observations and the CCSM4-1^o (see Figs. 14 and 15), although the warming reaches the equator and extends eastward sooner than in the original SFM hypothesis especially in the CCSM4-1^o.

We note that the NPO signature in DJF⁰ is associated with negative SST anomalies in the eastern equatorial Pacific and thus may in part reflect the ENSO cycle.

The SFM can also be evaluated directly based on wintertime SLP anomalies over the North Pacific. While the evolution of the SFM can be identified using the

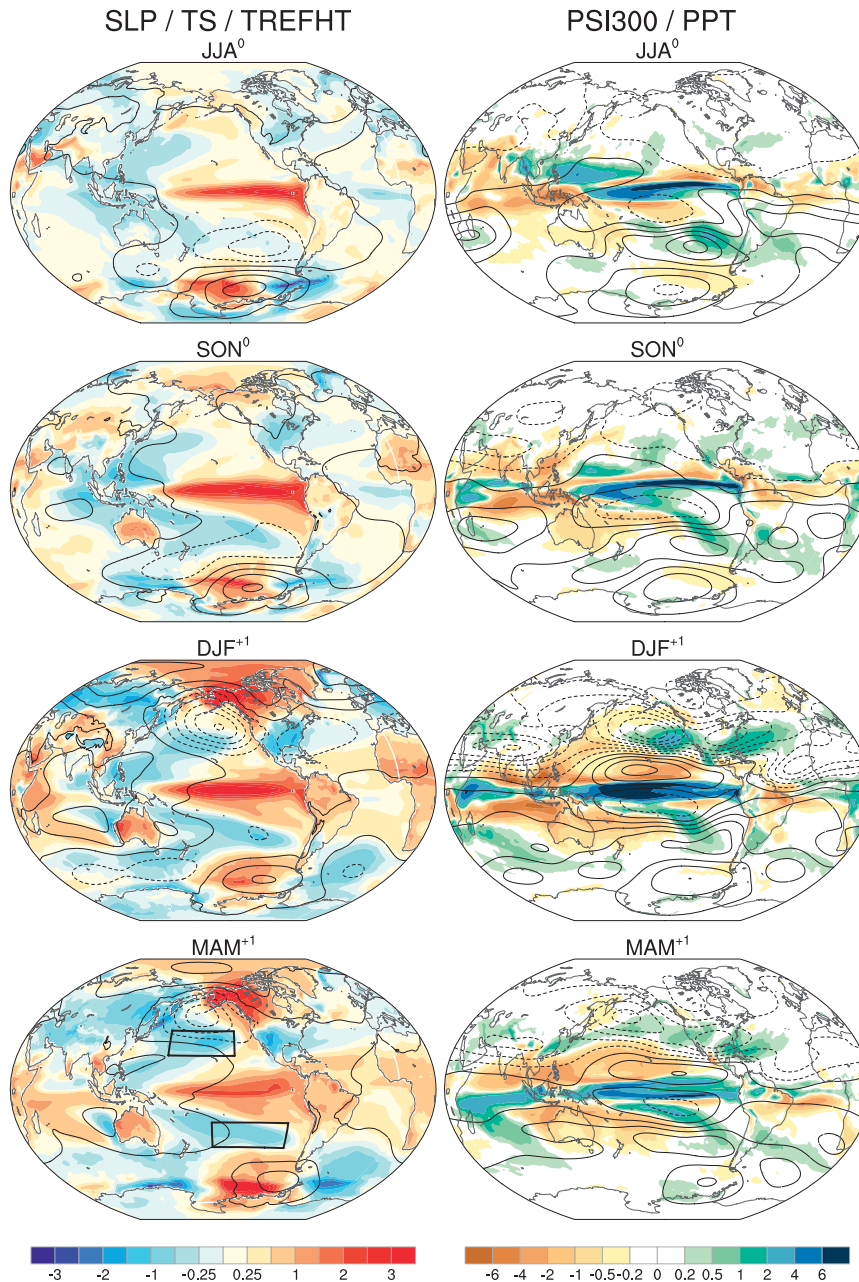


FIG. 15. As in Fig. 14, but for CCSM4-1°. The temperature anomalies are skin temperature over both land and ocean and thus also reflect the surface temperature over sea ice. The model composites have been scaled to match the observed composite amplitude of the Niño-3.4 SST index in Dec⁰. The boxes in the MAM⁺¹ panel outline the regions used for Fig. 16.

second PC of North Pacific SLP anomalies, Anderson (2003, 2007), Alexander et al. (2008), and Zhang et al. (2009) found that the SLP anomalies along the southeastern flank of the NPO was the key area for impacting the tropical Pacific. Following Anderson (2003) we construct an SLP index (SLPI) given by the normalized anomalies averaged over 10°–25°N, 175°–120°W (box in

top panels of Fig. 18) during Nov⁻¹–Mar⁰, to look for ENSO precursors. Seasonal composites of SLP and SST anomalies, shown in Fig. 18, are derived from the difference between fields averaged for when SLPI < -1 σ and when SLPI > +1 σ . In both the NCEP reanalysis and CCSM4-1°, the SLP composite difference during DJF⁰ (the middle 3 months of the SLP index) clearly

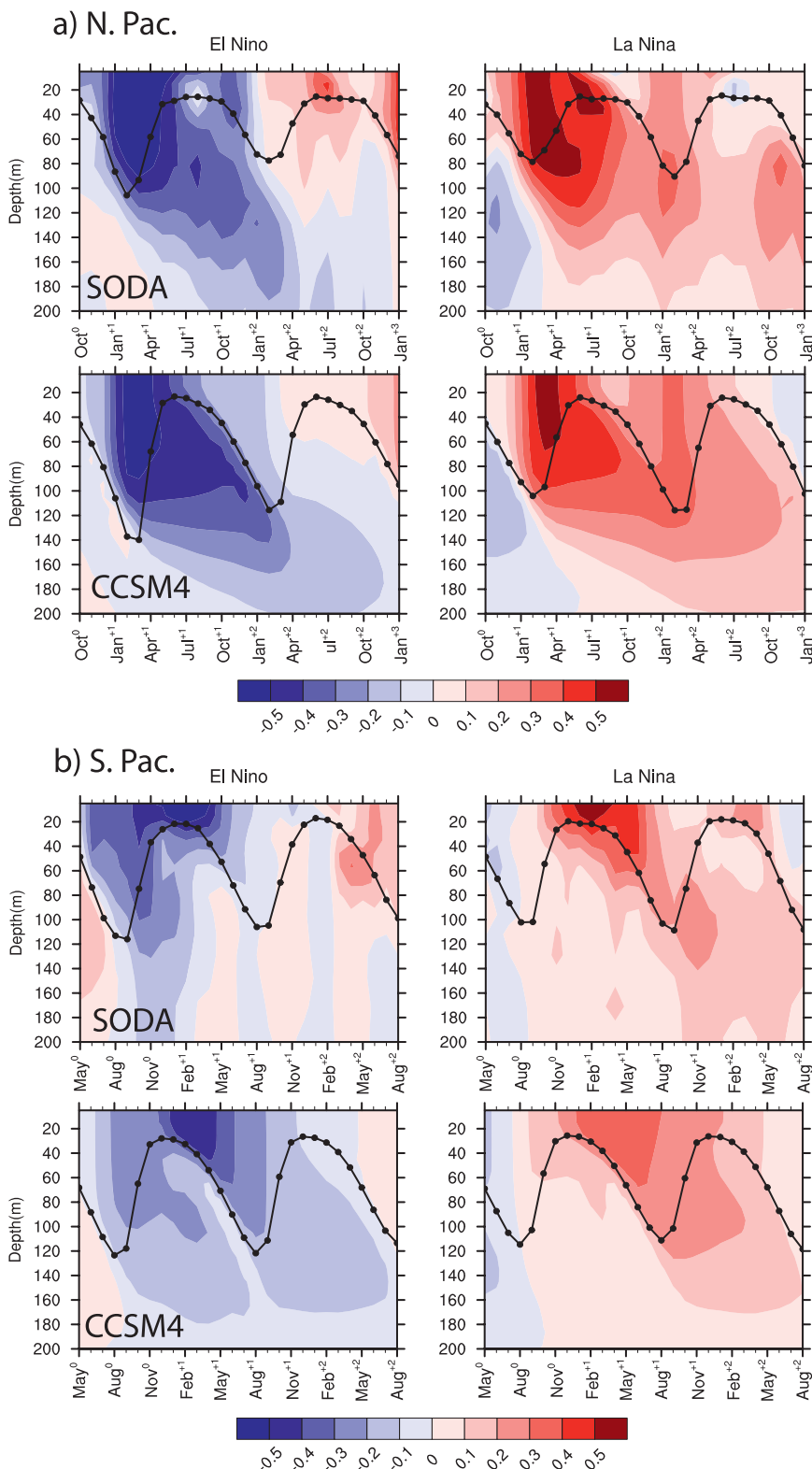


FIG. 16. (a) Time–depth sections of upper-ocean thermal anomalies (shading; °C) and mixed layer depth (black curves) for composite (left) El Niño and (right) La Niña events from SODA (1958–2007) and CCSM4–1° (model years 800–1300) for the central North Pacific. (b) As in (a), but for the central South Pacific. Regions outlined in Figs. 14 and 15. Note the different time axes in (a),(b).

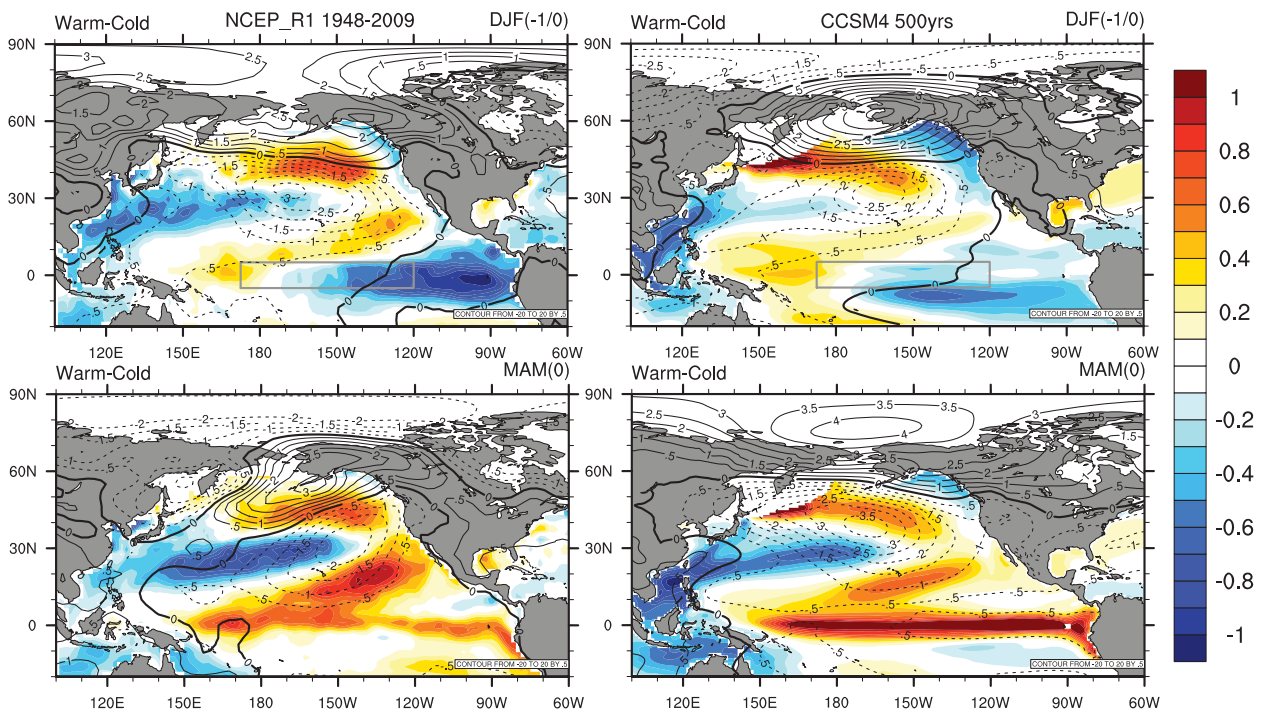


FIG. 17. El Niño – La Niña composites of SLP (contour interval is 1.0 hPa) and SST (shading interval is 0.1°C) anomalies for (top) DJF⁰ and (bottom) MAM⁰ from (left) NCEP–NCAR reanalysis (1948–2009) and (right) CCSM4–1° (model years 800–1300). Composites are based on the Niño 3.4 SST index in Dec⁰, approximately a year after the values shown in the top panel. Note that the model composites have not been scaled to match the observed composite amplitude of the Niño-3.4 SST index in Dec⁰. (top) Boxes indicate the Niño-3.4 index region.

depicts the NPO but with roughly twice the amplitude in CCSM4–1°. The SLP field is also very similar to the ENSO composite during DJF⁰ (top panels in Fig. 17). Note the year demarcation in Fig. 18 is relative to ENSO but the composites are only based on the SLPI and not whether an ENSO event occurs in the following winter.

Consistent with the SFM, anomalous southwesterly winds that oppose the climatological trade winds warm the underlying ocean via surface heat fluxes (not shown), creating positive SST anomalies in the index region in winter (Fig. 18). Positive SST anomalies, however, also develop along the equator between 150°E and 180° during DJF⁰ and spread eastward and amplify during MAM⁰ through SON⁰, strongly resembling the early phases of EN. Although the evolution of the SST field based on the SLPI is slightly faster and stronger in CCSM4–1° than in observations, the two are very similar and clearly related to ENSO as the correlation between the SLPI and Niño-3.4 SST index in JFM¹ is 0.61 in nature (Anderson 2007) and 0.59 in the model. The association between the NPO and negative SST anomalies in the eastern equatorial Pacific in DJF⁰ in both Figs. 17 and 18 raises the possibility that tropical forcing may contribute to the NPO precursor to ENSO. Additional analysis and targeted

modeling experiments are needed to investigate this issue further.

Anderson (2007) also found that the observed heat content in the western equatorial Pacific served as a precursor to ENSO but was most effective in combination with the subtropical SLP anomalies. Specifically, positive (negative) heat content anomalies associated with a deeper (shallower) thermocline in the western equatorial Pacific during JJA⁻¹ and SON⁻¹, 12–15 months before an ENSO event, followed by negative (positive) SLP anomalies over the subtropical central North Pacific during DJF⁰ favor EN (LN) events during the subsequent winter (DJF¹). When the two precursors have the same sign, their impact on ENSO is much weaker.

We explore the joint impact of these precursors on ENSO in CCSM4–1° through a scatterplot between the SLPI in Nov⁻¹–Mar⁰ and the Niño-3.4 index in JFM¹, stratified by whether an index of thermocline depth in the western equatorial Pacific [Z15I, the anomalous Z15 depth averaged over 5°N–5°S, 150°E–180° in June–October⁻¹ (JJASO⁻¹)] has the opposite or the same sign as the SLPI (Fig. 19a). We note that using Z20 in place of Z15 for the thermocline index yields virtually identical results as the two time series are correlated at 0.98. There is much less scatter and the magnitude of the correlation

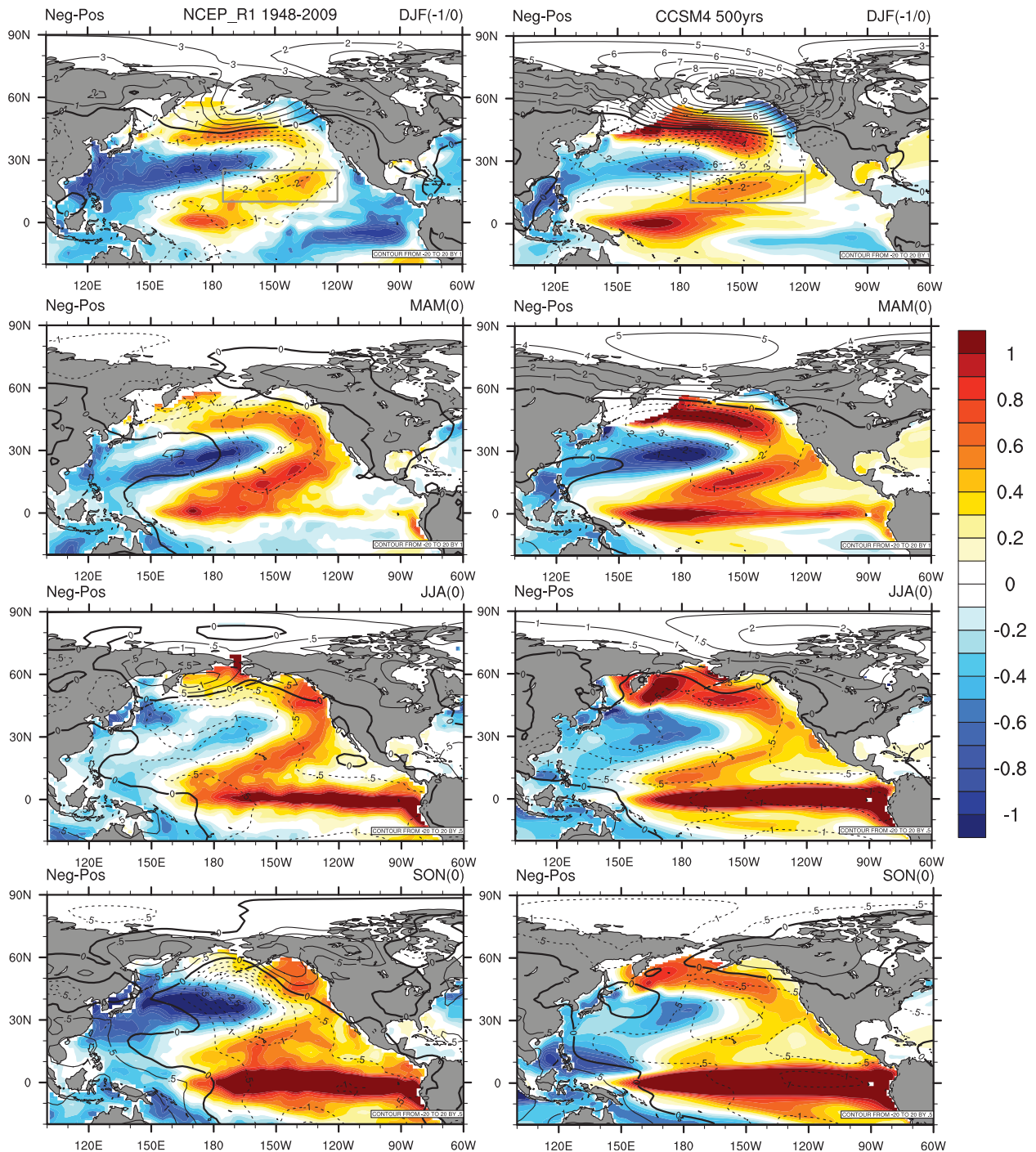


FIG. 18. Composites of SLP (contour interval is 1.0 hPa) and SST (shading interval is 0.1°C) anomalies for (top to bottom) DJF⁰, MAM⁰, JJA⁰, and SON⁰ based on the SLP index over the subtropical North Pacific (10°–25°N, 175°–120°W; see box in top panels) from (left) NCEP–NCAR reanalysis (1948–2009) and (right) CCSM4-1° (model years 800–1300). The composites are obtained by averaging the fields when SLP Index is ($< -1\sigma$) – ($> +1\sigma$). For consistency with Fig. 17, the seasons are labeled with respect to the timing of the ENSO cycle but an El Niño (La Niña) event is not required to follow a high (low) value of the SLP Index that was used to construct the composites.

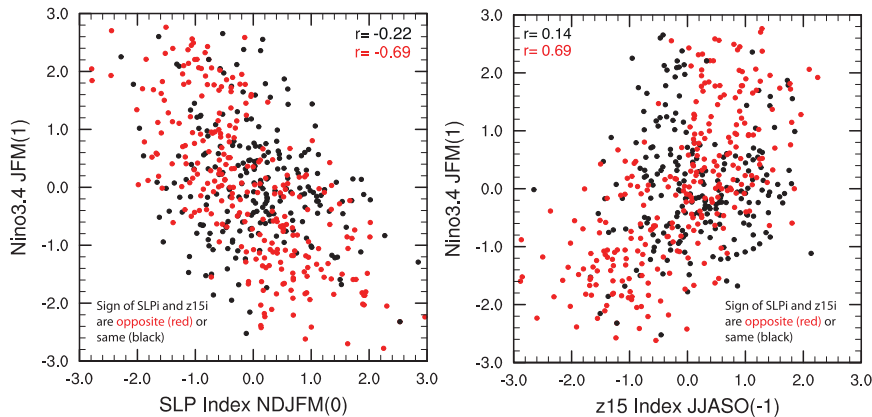


FIG. 19. (a) Scatterplot of the seasonal mean November–March subtropical North Pacific SLP index with the following year’s January–March Niño-3.4 index. Red (black) circles indicate the years in which the SLP index has the opposite (same) sign as thermocline depth anomalies averaged over the western equatorial Pacific (5°N – 5°S , 160°E – 180°) during the previous June–October (denoted Z15). (b) Scatterplot of the Z15 Index in JJASO^{-1} with the JFM^{+1} Niño-3.4 index 18 months later. Red (black) circles indicate those years in which the following year’s November–March SLP index has the opposite (same) sign as the Z15 Index.

between the Z15I and the Niño-3.4 index is high, -0.69 , when the SLPI is opposite to the Z15I, while the correlation is only -0.22 when the Z15I and SLPI anomalies have the same sign. These results are very similar to the observational results of Anderson (2007) who obtained correlations of -0.72 and -0.37 , respectively, in a comparable analysis. Likewise, the correlation between Z15I and the Niño-3.4 index in JFM^{+1} is strongly influenced by the SLPI: it is 0.69 when the SLPI and Z15I have the opposite sign and 0.14 when they have the same sign (Fig. 19b); Anderson obtained values of 0.69 and 0.06 from similar analyses of observations. These results suggest that the processes in the subtropical North Pacific involved in initiating ENSO events in CCSM4-1° are similar to those in nature and strongly depend on the state of the tropical Pacific.

b. PDV

As discussed in the introduction, PDV and ENSO exhibit similar spatial patterns of SST variability but with different regional emphasis (Zhang et al. 1997; Deser et al. 2010). These patterns are explicitly compared in Fig. 20a, which shows regression maps of monthly SST anomalies upon the leading PC time series of monthly SST anomalies over (left) the full Indo-Pacific domain (60°N – 60°S) and (right) the North Pacific domain (20° – 60°N) for HadISST during 1900–2010 (top), CCSM4-1° (middle), and CCSM3-T85 (bottom). The patterns based on the full Indo-Pacific depict the ENSO mode with largest amplitudes over the equatorial Pacific, while those based on the North Pacific define the PDO–PDV with maximum anomalies over the western and central

North Pacific. CCSM4-1° exhibits generally realistic ENSO and PDV spatial patterns, although the PDV connection to the tropical Pacific is weaker than observed and the maximum amplitude of the negative SST anomalies in the North Pacific occur directly east of Japan rather than in the central basin. In contrast, CCSM3-T85 exhibits negligible linkage between the tropical and extratropical Pacific for both ENSO and PDV.

Although their spatial patterns are similar, ENSO and PDV exhibit distinctive temporal behavior as reflected in their power spectra (Fig. 20b). ENSO is mainly an interannual mode of variability while PDV exhibits a predominantly red spectrum with maximum power at periods greater than ~ 10 yr in both observations and CCSM4-1° . It is interesting to note that the PDV mode may also be obtained as the leading EOF of 8-yr low-pass-filtered SST anomalies over the full Indo-Pacific domain (middle panel of Fig. 20a). The linkage between SST variability in the tropical and North Pacific on decadal and longer time scales in CCSM4-1° constitutes a notable improvement over CCSM3-T85 (Fig. 20a).

Subsurface temperature variations in the main thermocline of the North Pacific have been shown to be associated with PDV, both in observations (Deser et al. 1999; Schneider and Cornuelle 2005) and models (Latif and Barnett 1994; Kwon and Deser 2007; Zhong et al. 2008). Figure 21 (left panels) compares the leading EOF of annual (July–June) SST and 200-m-depth temperature (T_{200}) anomalies over the North Pacific in CCSM4-1° . The EOF patterns are broadly similar, with anomalies of one sign in the western and central North Pacific centered along the Kuroshio–Oyashio Extension (KOE) near 40°N ,

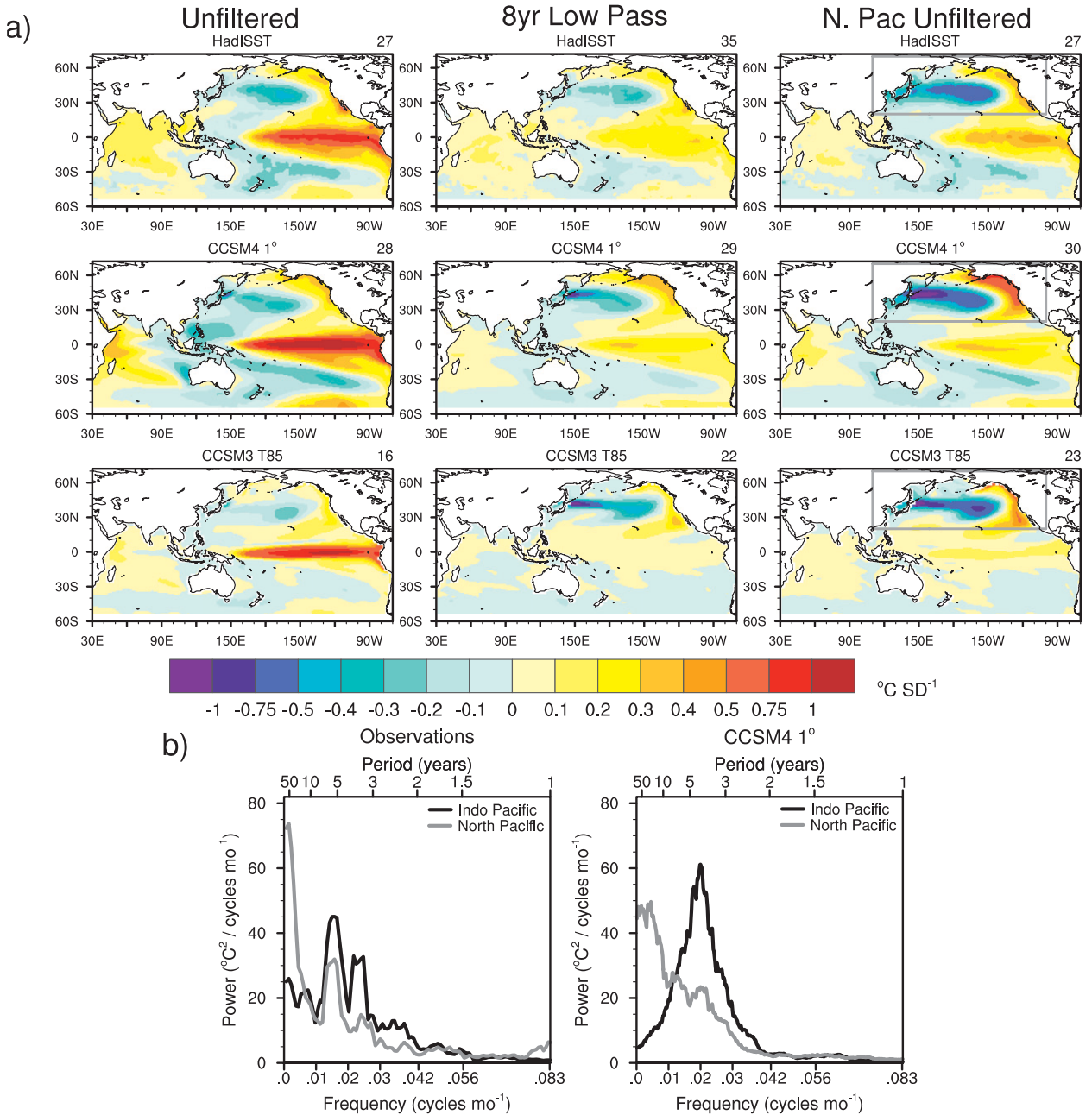


FIG. 20. (a) EOF1 of monthly SST anomalies for the full Indo-Pacific domain based on (left) unfiltered and (middle) 8-yr low-pass-filtered data, and (right) for the North Pacific domain (outlined by the box) based on unfiltered data for (top) HadISST 1900–2010, (middle) CCSM4–1° (model years 800–1300), and (bottom) CCSM3–T85 (model years 300–599). The results are shown as SST anomaly regressions upon the normalized PC time series (°C per standard deviation). The numbers at the top right corner of each panel denote the percent variance explained by the EOF (e.g., 27% for unfiltered HadISST over the full Indo-Pacific domain). (b) Power spectra of the unfiltered PC1 time series for the full Indo-Pacific domain (black curves) and the North Pacific domain (gray curves) from (left) HadISST and (right) CCSM4–1°.

surrounded by anomalies of the opposite sign to the north and east. The T200 EOF pattern in CCSM4–1° resembles that in SODA (not shown). Power spectra of the associated PC1 time series (right panels of Fig. 21) exhibit enhanced variance at periods longer than a decade, with a distinctive spectral peak 12~18 yr (hereafter referred

to as the nominal 15-yr oscillation) that is statistically significant at the 99% (~95%) confidence level relative to a first-order autoregressive model for T200 (SST). A secondary spectral peak of ~40 yr is evident for T200, but it is not significant with respect to a first-order autoregressive model. The two PC time series are highly

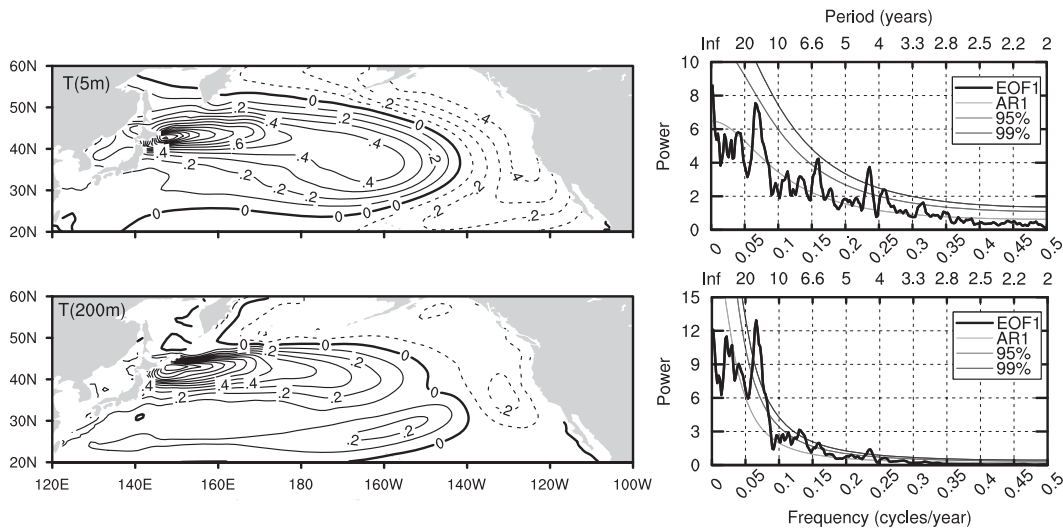


FIG. 21. (left) EOF1 of annual (July–June) temperature anomalies at (top) the sea surface and (bottom) 200-m depth over the North Pacific from CCSM4-1° (model years 800–1299). The EOF accounts for 40% (31%) of the variance at 5 m (200 m). (right) Power spectra of the PC1 time series (thick black curve) and of the best-fit first-order autoregressive process and associated 95% and 99% confidence limits (thin gray curves).

correlated ($r = 0.87$ when SST leads T200 by 1 yr). It is interesting to note that similar low-frequency peaks were also found in CCSM2 and CCSM3 (Alexander et al. 2006; Kwon and Deser 2007; Zhong et al. 2008).

To understand the role of the atmosphere in North Pacific Ocean decadal variability, we regress 10-yr low-pass-filtered annual (July–June) SLP, precipitation, wind stress curl, and SST anomalies upon the normalized 10-yr low-pass-filtered T200 PC1, lagging the PC1 record by 3 yr to capture the strongest associations between the atmospheric fields and T200 PC1 as will be discussed further below (Fig. 22). The lag regression maps indicate that positive SLP and anticyclonic (negative) wind stress curl anomalies over the North Pacific precede positive 200-m-depth temperature anomalies along the KOE by 3 yr. These atmospheric patterns and the 3-yr delay are qualitatively consistent with the mechanism of oceanic Rossby wave adjustment (e.g., Deser et al. 1999; Schneider and Cornuelle 2005; Kwon and Deser 2007). The SST anomaly pattern that occurs in association with T200 PC1 3 years later resembles the leading EOF of North Pacific SST (Fig. 21). Multiple processes may be responsible for the SST regression pattern, including direct atmospheric forcing of the ocean mixed layer via turbulent and radiative energy fluxes and Ekman advection, as well as ocean circulation effects through lateral geostrophic heat flux convergence and entrainment of subsurface ocean temperature anomalies (e.g., Kwon and Deser 2007; Kwon et al. 2010). In addition to changes over the North Pacific, both the precipitation and SST regression maps exhibit significant anomalies

within the tropics. In particular, negative precipitation anomalies are found over the western equatorial Pacific extending eastward along the off-equatorial intertropical convergence zones (ITCZs). These tropical precipitation anomalies occur in association with negative SST anomalies in the western equatorial Pacific “Niño-4” region (5°N–5°S, 160°E–150°W).

To further examine the lead–lag relationships among the different fields, and to validate our choice of 3-yr lag in Fig. 22, we computed the lag-correlation curves between the T200 PC1 and the “North Pacific SLP index” (NPI; Trenberth and Hurrell 1994) defined as the average SLP over the region (30°–65°N, 160°E–140°W), and between the T200 PC1 and the “Niño-4” SST index based on 10-yr low-pass-filtered data (Fig. 23). The maximum correlation coefficients (significant at the 99% level taking into account the autocorrelations in the two records) between T200 PC1 and the NPI occur when the atmosphere leads the ocean by 1–4 yr, with a peak value of 0.63 at 3 yr. The approximate 15-yr periodicity is also evident in the NPI-T200 PC1 lag-correlation curve. In contrast, the lag-correlation curve between the inverted “Niño-4” SST index and T200 PC1 does not show the 15-yr periodicity, but does show a maximum correlation (0.51; significant at the 99% level taking into account the autocorrelations in the two records) when the “Niño-4” SST index leads the T200 PC1 by 2 yr.

To examine whether the atmospheric circulation may respond significantly to SST anomalies associated with PDV, we show the unfiltered regression maps of SLP, SST, and wind stress curl over the North Pacific upon the

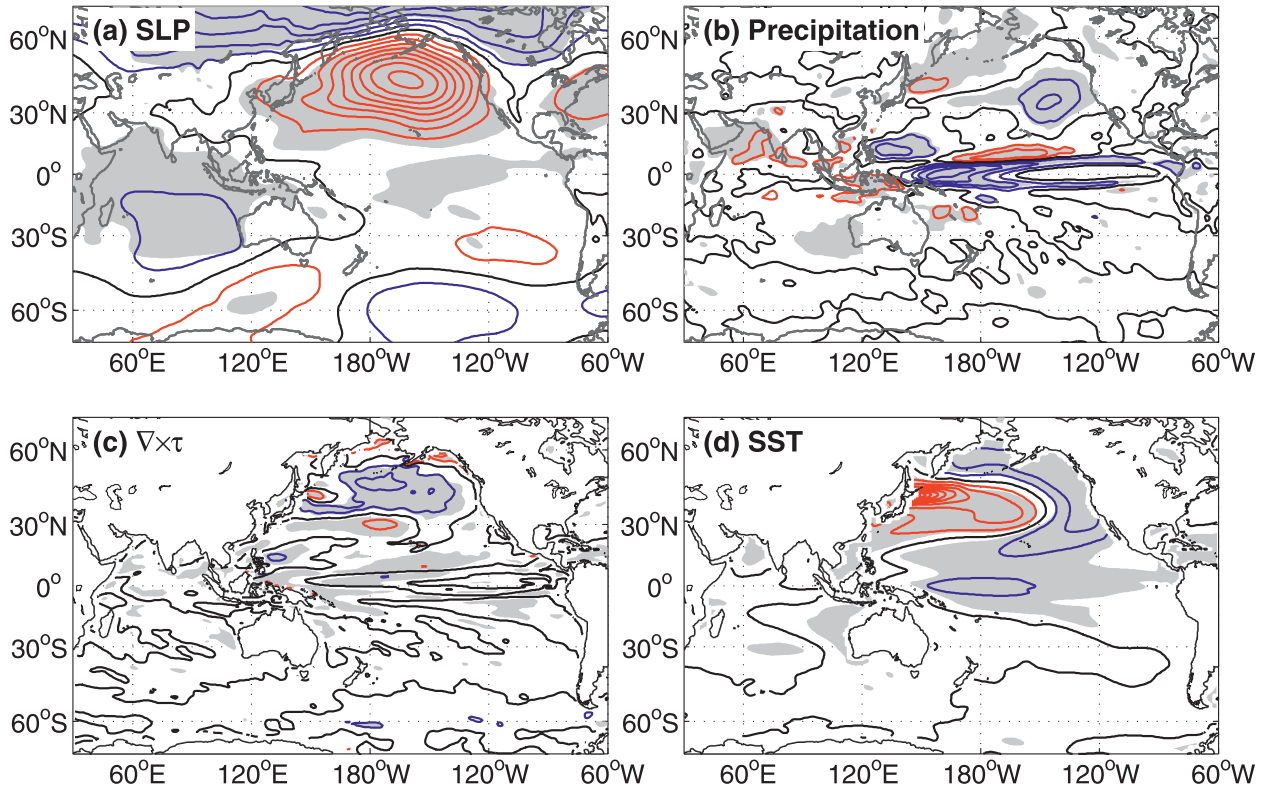


FIG. 22. Lag regressions of July–June (a) sea level pressure, (b) precipitation, (c) wind stress curl, and (d) SST anomalies on the leading PC time series of July–June 200-m temperature in the North Pacific when the PC time series lags by 3 yr. All variables are low-pass filtered to retain periods longer than 10 yr. Contour intervals are 0.1 hPa, 0.1 mm day⁻¹, 0.5×10^{-8} N m⁻³, and 0.1°C, respectively. Positive (negative) contours are in red (blue), and the 0 contour is in black. Gray shading indicates regression values significant at the 95% confidence level.

unfiltered T200 PC1 time series at lags +1, 0, and -1 yr (Fig. 24). The reason for examining the unfiltered regressions is to separate the relatively fast (order several weeks; Deser et al. 2007; Ferreira and Frankignoul 2005, 2008) atmospheric response from the relatively slow atmospheric forcing of the ocean (order several years due to midlatitude Rossby wave adjustment processes; Frankignoul et al. 1997). We further isolate the response to North Pacific SST anomalies by removing covariability with the first 3 EOFs of tropical Indo-Pacific SST anomalies through multiple linear regression (Frankignoul et al. 2011). The results show that the atmospheric circulation anomalies undergo a rapid change in sign between +1- and -1-yr lag, such that the spatially extensive positive SLP and negative wind stress curl regressions when the atmosphere leads the subsurface ocean by 1 yr are replaced by statistically significant regressions of the opposite sign localized to the region of positive SST anomalies along the KOE when the atmosphere lags the subsurface ocean by 1 yr (Fig. 24). The vertical structure of the atmospheric circulation also changes from equivalent barotropic at -1-yr lag to baroclinic at +1-yr lag

(not shown). We note that the simultaneous regressions contain signatures of both atmospheric forcing and response.

The characteristics of PDV, defined as the leading EOF of North Pacific T200, in CCSM4-1° exhibit many similarities with those in CCSM2 and CCSM3, including the patterns of atmospheric forcing and response (Alexander et al. 2006; Kwon and Deser 2007; Zhong et al. 2008; Kwon et al. 2010). In these studies, PDV was interpreted as a weakly damped coupled ocean-atmosphere oscillation intrinsic to the North Pacific in which basin-scale stochastic atmospheric forcing drives a delayed oceanic response via Rossby wave adjustment processes. The associated changes in oceanic lateral heat flux convergence along the KOE in turn force SST anomalies that drive a weak atmospheric response needed to sustain the oscillation. However, unlike CCSM2, PDV in CCSM4-1° also shows significant associations with the tropics, in particular SST and precipitation anomalies in the western equatorial Pacific. The role of the tropical Pacific in modifying and responding to North Pacific PDV remains to be investigated.

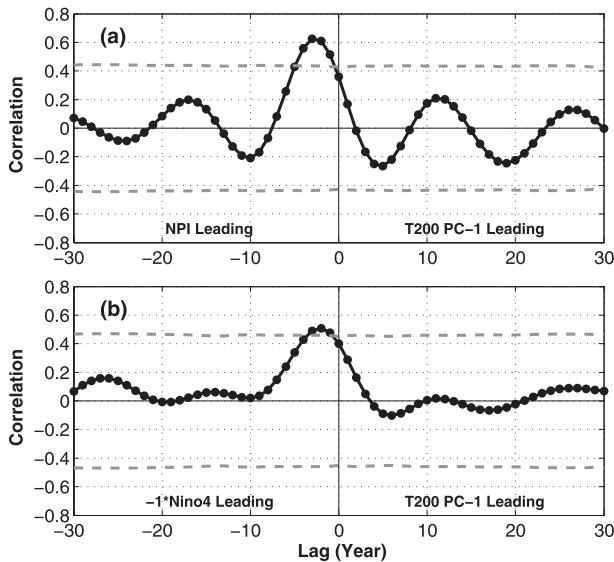


FIG. 23. Lag correlation between the leading PC time series of July–June 200-m temperature in the North Pacific and the July–June (a) North Pacific SLP index (NPI; 30°–65°N, 160°E–140°W) and (b) the inverted Niño-4 SST index (5°S–5°N, 160°E–150°W). All time series are 10-yr low-pass filtered before computing the correlations. Dashed lines indicate the 99% significance level taking into account autocorrelation in each record.

4. Summary and outstanding issues

We have given an overview of ENSO and PDV in the 1300-yr preindustrial control integration of CCSM4 at 1° resolution. Several aspects of ENSO are improved in CCSM4-1° compared to its predecessor CCSM3-T85, including the lengthened period (3–6 yr), the larger range of amplitude and frequency of events, and the longer duration of La Niña compared to El Niño. However, the amplitude of Niño-3.4 SST variability is overestimated by approximately 30%, with a standard deviation of 1.06°C compared to 0.75°C for observations and 0.80°C for CCSM3-T85. In addition, although the degree of ENSO irregularity is improved in CCSM4-1° compared to CCSM3-T85, it is still smaller than in nature. Like CCSM3-T85, ENSO in CCSM4-1° exhibits characteristics consistent with the delayed-recharge oscillator paradigm, and within this framework the lengthened period is consistent with the increased latitudinal width of the anomalous equatorial zonal wind stress. CCSM4-1° generally simulates realistic global atmospheric circulation teleconnections to ENSO with accompanying impacts on precipitation and temperature, although the wintertime deepening of the Aleutian low erroneously persists into spring. The late winter extratropical SST response to these teleconnections is substantially improved in CCSM4-1° compared to CCSM3-T85, both in pattern and magnitude. The vertical structure and

seasonal evolution of the upper-ocean temperature response in the North and South Pacific is generally well simulated, including asymmetries between warm and cold events. The model’s ENSO shows evidence of atmospheric circulation precursors over the North Pacific associated with the “seasonal footprinting mechanism”, similar to observations. The spatial structure of PDV in CCSM4-1°, determined from EOF analysis of upper-ocean temperature anomalies over the North Pacific, is generally realistic except for the weaker amplitude within the tropics and overly strong variability east of Japan along the KOE and represents a substantial improvement over CCSM3-T85. This mode exhibits a significant spectral peak at approximately 15 yr.

Numerous aspects of ENSO and PDV in CCSM4-1° remain to be investigated. In particular, the role of the Madden–Julian oscillation (MJO) and westerly wind bursts in the initiation and maintenance of ENSO events should be examined as was done for CCSM3.5 (Neale et al. 2008). We note that the simulation of the MJO is substantially improved in CCSM4-1° when compared to CCSM3 (Subramanian et al. 2011). Similarly, additional analysis is needed regarding the role of the SFM in triggering ENSO events from both the North and South Pacific, and to what extent this mechanism reflects stochastic atmospheric variability or is intrinsic to the ENSO cycle. The mechanisms responsible for the large range of ENSO behavior in CCSM4-1° remain to be understood, including whether it is randomly generated as in the GFDL CM2.1 model (Wittenberg 2009), or whether decadal variability within the tropical Pacific due to dynamical and thermodynamic air–sea interaction (Clement et al. 2011) and the nonlinear rectification of warm and cold events (e.g., Rodgers et al. 2004) are also important. Similarly, the mechanisms underlying the extended duration of cold events compared to warm events in CCSM4-1° need to be clarified and assessed for relevance to nature. Additional analysis of the upper-ocean thermal response to ENSO in the extratropical oceans, including the consequences of the asymmetric temperature response beneath the mixed layer during EN compared to LN, would also be worthwhile. Finally, a more in-depth characterization and mechanistic understanding of the model’s PDV including patterns beyond the leading EOF and the role of tropical–extratropical coupling remain outstanding issues. To date, model simulations have been equivocal concerning changes in amplitude or frequency of ENSO events in response to increases in greenhouse gas concentrations (Guilyardi et al. 2009). Given the large natural range of ENSO variability in CCSM4-1°, detection of an externally forced change in ENSO behavior will be a challenging endeavor (Stevenson et al. 2012).

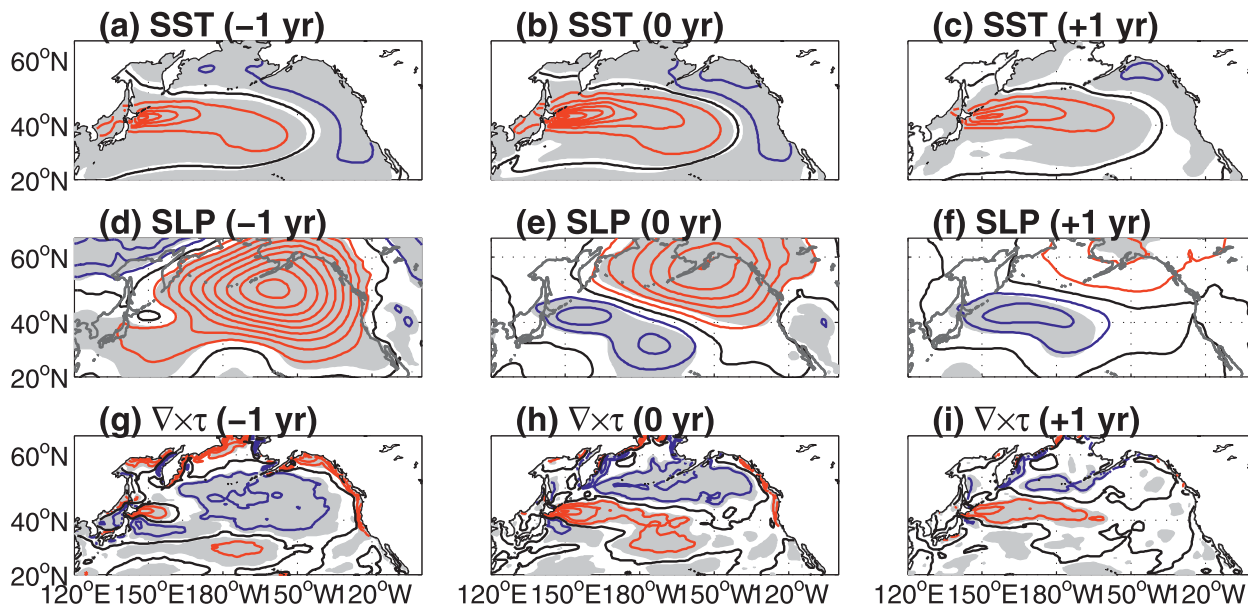


FIG. 24. The (left to right) -1 , 0 , and $+1$ lag regressions of July–June (a)–(c) SST, (d)–(f) SLP, and (g)–(i) wind stress curl anomalies on the leading PC time series of July–June 200-m temperature in the North Pacific. Negative (positive) lag indicates the PC lags (leads) the regressed field. Note that covariability with the first three EOFs of tropical Indo-Pacific (12.5°S – 12.5°N) SST anomalies have been removed before the regressions are calculated. Contour intervals are 0.2°C , 0.1 hPa, and $0.5 \times 10^{-8} \text{ N m}^{-3}$, respectively. Positive (negative) contours are in red (blue), and the 0 contour is in black. Gray shading indicates regression values significant at the 95% confidence level. No time filtering has been applied to any of the data records.

Acknowledgments. We thank the anonymous reviewers and the editor for their constructive comments. M. Alexander, A. Capotondi, and J. Scott's participation was supported by a grant from the NSF Climate and Large-scale Dynamics Program. Y.-O. Kwon gratefully acknowledges support from a WHOI Heyman fellowship and a grant from the NSF Climate and Large-scale Dynamics Program. The CESM project is supported by the National Science Foundation and the Office of Science (BER) of the U.S. Department of Energy. Computing resources were provided by the Climate Simulation Laboratory at NCAR's Computational and Information Systems Laboratory (CISL), sponsored by the National Science Foundation and other agencies. NCAR is sponsored by the National Science Foundation.

REFERENCES

- Adler, R. F., and Coauthors, 2003: The Version-2 Global Precipitation Climatology Project (GPCP) monthly precipitation analysis (1979–present). *J. Hydrometeor.*, **4**, 1147–1167.
- Alexander, M. A., 2010: Extratropical air–sea interaction, sea surface temperature variability, and the Pacific decadal oscillation. *Climate Dynamics: Why Does Climate Vary?*, *Geophys. Monogr.*, Vol. 189, Amer. Geophys. Union, 123–148.
- , and C. Deser, 1995: A mechanism for the recurrence of midlatitude SST anomalies during winter. *J. Phys. Oceanogr.*, **25**, 122–137.
- , M. S. Timlin, and J. D. Scott, 2001: Winter-to-winter recurrence of sea surface temperature, salinity, and mixed layer depth anomalies. *Prog. Oceanogr.*, **49**, 41–61.
- , I. Blade, M. Newman, J. Lanzante, N.-C. Lau, and J. D. Scott, 2002: The atmospheric bridge: The influence of ENSO teleconnections on air–sea interaction over the global oceans. *J. Climate*, **15**, 2205–2231.
- , and Coauthors, 2006: Extratropical atmosphere–ocean variability in the CCSM3. *J. Climate*, **19**, 2496–2525.
- , L. Matrosova, C. Penland, J. D. Scott, and P. Chang, 2008: Forecasting Pacific SSTs: Linear inverse model predictions of the PDO. *J. Climate*, **21**, 385–402.
- , D. J. Vimont, P. Chang, and J. D. Scott, 2010: The impact of extratropical atmospheric variability on ENSO: Testing the seasonal footprinting mechanism using coupled model experiments. *J. Climate*, **23**, 2885–2901.
- An, S.-I., and B. Wang, 2000: Interdecadal change of the structure of the ENSO mode and its impact on the ENSO frequency. *J. Climate*, **13**, 2044–2055.
- Anderson, B. T., 2003: Tropical Pacific sea surface temperatures and preceding sea level pressure anomalies in the subtropical North Pacific. *J. Geophys. Res.*, **108**, 4732, doi:10.1029/2003JD003805.
- , 2004: Investigation of a large-scale mode of ocean–atmosphere variability and its relation to tropical Pacific sea surface temperature anomalies. *J. Climate*, **17**, 4089–4098.
- , 2007: On the joint role of subtropical atmospheric variability and equatorial subsurface heat content anomalies in initiating the onset of ENSO events. *J. Climate*, **20**, 926–936.
- , and E. Maloney, 2006: Interannual tropical Pacific sea surface temperatures and preceding subtropical North Pacific sea level pressure anomalies in the NCAR CCSM2.0. *J. Climate*, **19**, 998–1012.

- Barlow, M., S. Nigam, and E. H. Berbery, 2001: ENSO, Pacific decadal variability, and U.S. summertime precipitation, drought, and stream flow. *J. Climate*, **14**, 2105–2128.
- Brohan, P., J. J. Kennedy, I. Harris, S. F. B. Tett, and P. D. Jones, 2006: Uncertainty estimates in regional and global observed temperature changes: A new dataset from 1850. *J. Geophys. Res.*, **111**, D12106, doi:10.1029/2005JD006548.
- Capotondi, A., 2008: Can the mean structure of the tropical pycnocline affect ENSO period in coupled climate models? *Ocean Modell.*, **20**, 157–169.
- , A. Wittenberg, and S. Masina, 2006: Spatial and temporal structure of tropical Pacific interannual variability in 20th century climate simulations. *Ocean Modell.*, **15**, 274–298.
- Carton, J. A., and B. S. Giese, 2008: A reanalysis of ocean climate using Simple Ocean Data Assimilation (SODA). *Mon. Wea. Rev.*, **136**, 2999–3017.
- Chang, P., and Coauthors, 2006: Climate fluctuations of tropical coupled systems—The role of ocean dynamics. *J. Climate*, **19**, 5122–5174.
- Clement, A., P. DiNezio, and C. Deser, 2011: Rethinking the ocean's role in the Southern Oscillation. *J. Climate*, **24**, 4056–4072.
- Danabasoglu, G., S. Bates, B. P. Briegleb, S. R. Jayne, M. Jochum, W. G. Large, S. Peacock, and S. G. Yeager, 2012: The CCSM4 ocean component. *J. Climate*, **25**, 1361–1389.
- Deser, C., and M. L. Blackmon, 1995: On the relationship between tropical and North Pacific sea surface temperature variations. *J. Climate*, **8**, 1677–1680.
- , M. A. Alexander, and M. S. Timlin, 1999: Evidence for a wind-driven intensification of the Kuroshio Current Extension from the 1970s to the 1980s. *J. Climate*, **12**, 1697–1706.
- , —, and —, 2003: Understanding the persistence of sea surface temperature anomalies in midlatitudes. *J. Climate*, **16**, 57–72.
- , A. S. Phillips, and J. W. Hurrell, 2004: Pacific interdecadal climate variability: Linkages between the tropics and the North Pacific during boreal winter since 1900. *J. Climate*, **17**, 3109–3124.
- , A. Capotondi, R. Saravanan, and A. S. Phillips, 2006: Tropical Pacific and Atlantic climate variability in CCSM3. *J. Climate*, **19**, 2451–2481.
- , R. A. Tomas, and S. Peng, 2007: The transient atmospheric circulation response to North Atlantic SST and sea ice anomalies. *J. Climate*, **20**, 4751–4767.
- , M. A. Alexander, S.-P. Xie, and A. S. Phillips, 2010: Sea surface temperature variability: Patterns and mechanisms. *Annu. Rev. Mar. Sci.*, **2**, 115–143, doi:10.1146/annurev-marine-120408-151453.
- Di Lorenzo, E., and Coauthors, 2008: North Pacific Gyre Oscillation links ocean climate and ecosystem change. *Geophys. Res. Lett.*, **35**, L08607, doi:10.1029/2007GL032838.
- Ferreira, D., and C. Frankignoul, 2005: The transient atmospheric response to midlatitude SST anomalies. *J. Climate*, **18**, 1049–1067.
- , and —, 2008: Transient atmospheric response to interactive SST anomalies. *J. Climate*, **21**, 576–583.
- Frankignoul, C., P. Muller, and E. Zorita, 1997: A simple model of the decadal response of the ocean to stochastic wind forcing. *J. Phys. Oceanogr.*, **27**, 1533–1546.
- , N. Sennéchal, Y.-O. Kwon, and M. A. Alexander, 2011: At Influence of the meridional shifts of the Kuroshio and the Oyashio Extensions on the atmospheric circulation. *J. Climate*, **24**, 762–777.
- Gent, P. R., and Coauthors, 2011: The Community Climate System Model version 4. *J. Climate*, **24**, 4973–4991.
- Glantz, M. H., 2000: *Currents of Change: El Niño and La Niña Impacts on Climate and Society*. Cambridge University Press, 252 pp.
- Guan, B., and S. Nigam, 2008: Pacific sea surface temperatures in the twentieth century: An evolution-centric analysis of variability and trend. *J. Climate*, **21**, 2790–2809.
- Guilyardi, E., A. Wittenberg, A. Fedorov, M. Collins, C. Wang, A. Capotondi, G. J. van Oldenborgh, and T. Stockdale, 2009: Understanding El Niño in ocean–atmosphere general circulation models: Progress and challenges. *Bull. Amer. Meteor. Soc.*, **90**, 325–340.
- Harrison, D. E., and N. K. Larkin, 1998: El Niño–Southern Oscillation sea surface temperature and wind anomalies. *Rev. Geophys.*, **36**, 353–399.
- Jin, D., and B. P. Kirtman, 2009: Why the Southern Hemisphere ENSO responses lead ENSO. *J. Geophys. Res.*, **114**, D23101, doi:10.1029/2009JD012657.
- Jin, F.-F., 1997a: An equatorial ocean recharge paradigm for ENSO. Part I: Conceptual model. *J. Atmos. Sci.*, **54**, 811–829.
- , 1997b: An equatorial ocean recharge paradigm for ENSO. Part II: A stripped-down coupled model. *J. Atmos. Sci.*, **54**, 830–847.
- Kalnay, E., and Coauthors, 1996: The NCEP/NCAR 40-Year Reanalysis Project. *Bull. Amer. Meteor. Soc.*, **77**, 437–471.
- Kirtman, B. P., 1997: Oceanic Rossby wave dynamics and the ENSO period in a coupled model. *J. Climate*, **10**, 1690–1704.
- Kleeman, R., J. P. McCreary, and B. A. Klinger, 1999: A mechanism for the decadal variation of ENSO. *Geophys. Res. Lett.*, **26**, 1743–1747.
- Kwon, Y.-O., and C. Deser, 2007: North Pacific decadal variability in the Community Climate System Model version 2. *J. Climate*, **20**, 2416–2433.
- , —, and C. Cassou, 2010: Coupled atmosphere – mixed layer ocean response to ocean heat flux convergence along the Kuroshio Current Extension. *Climate Dyn.*, **36**, 2295–2312, doi:10.1007/s00382-010-0764-8.
- Latif, M., and T. P. Barnett, 1994: Causes of decadal climate variability over the North Pacific and North America. *Science*, **266**, 634–637.
- Li, J., and Coauthors, 2011: Interdecadal modulation of El Niño amplitude during the past millennium. *Nat. Climate Change*, **1**, 114–118.
- Lin, S. J., 2004: A “vertically Lagrangian” finite-volume dynamical core for global models. *Mon. Wea. Rev.*, **132**, 2293–2307.
- Linkin, M. E., and S. Nigam, 2008: The North Pacific Oscillation–west Pacific teleconnection pattern: Mature-phase structure and winter impacts. *J. Climate*, **21**, 1979–1997.
- Mantua, N. J., S. R. Hare, Y. Zhang, J. M. Wallace, and R. C. Francis, 1997: A Pacific interdecadal oscillation with impacts on salmon production. *Bull. Amer. Meteor. Soc.*, **78**, 1069–1079.
- Meinen, C. S., and M. J. McPhaden, 2000: Observations of warm water volume changes in the equatorial Pacific and their relationship to El Niño and La Niña. *J. Climate*, **13**, 3551–3559.
- Minobe, S., 1997: A 50–70 year climatic oscillation over the North Pacific and North America. *Geophys. Res. Lett.*, **24**, 683–686.
- , 1999: Resonance in bidecadal and pentadecadal climate oscillations over the North Pacific: Role in climatic regime shifts. *Geophys. Res. Lett.*, **26**, 855–858.
- Nakamura, H., H. G. Lin, and T. Yamagata, 1997: Decadal climate variability in the North Pacific in recent decades. *Bull. Amer. Meteor. Soc.*, **78**, 2215–2226.
- Neale, R. B., J. H. Richter, and M. Jochum, 2008: The impact of convection of ENSO: From a delayed oscillator to a series of events. *J. Climate*, **21**, 5904–5924.

- Neelin, J. D., D. S. Battisti, A. C. Hirst, F.-F. Jin, Y. Wakata, T. Yamagata, and S. E. Zebiak, 1998: ENSO theory. *J. Geophys. Res.*, **103**, 14 261–14 290.
- Newman, M., G. Compo, and M. A. Alexander, 2003: ENSO-forced variability of the Pacific decadal oscillation. *J. Climate*, **16**, 3853–3857.
- Ohba, M., and H. Ueda, 2009: Role of nonlinear atmospheric response to SST on the asymmetric transition process of ENSO. *J. Climate*, **22**, 177–192.
- Okumura, Y. M., and C. Deser, 2010: Asymmetry in the duration of El Niño and La Niña. *J. Climate*, **23**, 5826–5843.
- Philander, S. G., 1990: *El Niño, La Niña and the Southern Oscillation*. Academic Press, 293 pp.
- Pierce, D. W., 2001: Distinguishing coupled ocean–atmosphere interactions from background noise in the North Pacific. *Prog. Oceanogr.*, **49**, 331–352.
- , T. P. Barnett, and M. Latif, 2000: Connections between the Pacific Ocean tropics and midlatitudes on decadal timescales. *J. Climate*, **13**, 1173–1194.
- Power, S. B., T. Casey, C. Folland, A. Colman, and V. Mehta, 1999: Interdecadal modulation of the impact of ENSO on Australia. *Climate Dyn.*, **15**, 319–324.
- Qiu, B., N. Schneider, and S. Chen, 2007: Coupled variability in the North Pacific: Observationally constrained idealized model. *J. Climate*, **20**, 3602–3620.
- Rayner, N. A., D. E. Parker, E. B. Horton, C. K. Folland, L. V. Alexander, D. P. Rowell, E. C. Kent, and A. Kaplan, 2003: Global analyses of sea surface temperature, sea ice, and night marine air temperature since the late nineteenth century. *J. Geophys. Res.*, **108**, 4407, doi:10.1029/2002JD002670.
- Richter, J. H., and P. J. Rasch, 2008: Effects of convective momentum transport on the atmospheric circulation in the Community Atmosphere Model, version 3 (CAM3). *J. Climate*, **21**, 1487–1499.
- Rodgers, K. B., P. Friederichs, and M. Latif, 2004: Tropical Pacific decadal variability and its relation to decadal modulation of ENSO. *J. Climate*, **17**, 3761–3774.
- Rogers, J. C., 1981: The North Pacific Oscillation. *J. Climatol.*, **1**, 39–52.
- Ropelewski, C. F., and M. S. Halpert, 1987: Global- and regional-scale precipitation patterns associated with the El Niño/Southern Oscillation. *Mon. Wea. Rev.*, **115**, 1606–1626.
- Schneider, N., and B. D. Cornuelle, 2005: The forcing of the Pacific decadal oscillation. *J. Climate*, **18**, 4355–4357.
- Schott, F. A., S.-P. Xie, and J. P. McCreary, 2009: Indian Ocean circulation and climate variability. *Rev. Geophys.*, **47**, RG1002, doi:10.1029/2007RG000245.
- Shakun, J. D., and J. Shaman, 2009: Tropical origins of North and South Pacific decadal variability. *Geophys. Res. Lett.*, **36**, L19711, doi:10.1029/2009GL040313.
- Spencer, H., and J. M. Slingo, 2003: The simulation of peak and delayed ENSO teleconnections. *J. Climate*, **16**, 1757–1774.
- Stevenson, S., B. Fox-Kemper, M. Jochum, B. Rajagopalan, and S. Yeager, 2010: Model ENSO validation using wavelet probability analysis. *J. Climate*, **23**, 5540–5547.
- , —, —, R. Neale, C. Deser, and G. Meehl, 2012: Will there be a significant change to El Niño in the twenty-first century? *J. Climate*, **25**, 2129–2145.
- Subramanian, A. C., M. Jochum, A. J. Miller, R. Murtugudde, R. B. Neale, and D. E. Waliser, 2011: The Madden–Julian oscillation in CCSM4. *J. Climate*, **24**, 6261–6282.
- Tippett, M. K., and A. G. Barnston, 2008: Skill of multimodel ENSO probability forecasts. *Mon. Wea. Rev.*, **136**, 3933–3946.
- Trenberth, K. E., and J. W. Hurrell, 1994: Decadal atmosphere–ocean variations in the Pacific. *Climate Dyn.*, **9**, 303–319.
- , G. W. Branstator, D. Karoly, A. Kumar, N.-C. Lau, and C. Ropelewski, 1998: Progress during TOGA in understanding and modeling global teleconnections associated with tropical sea surface temperatures. *J. Geophys. Res.*, **103**, 14 291–14 324.
- , J. M. Caron, D. P. Stepaniak, and S. Worley, 2002: Evolution of El Niño–Southern Oscillation and global atmospheric surface temperatures. *J. Geophys. Res.*, **107**, 4065, doi:10.1029/2000JD000298.
- Vimont, D. J., 2005: The contribution of the interannual ENSO cycle to the spatial pattern of ENSO-like decadal variability. *J. Climate*, **18**, 2080–2092.
- , S. Battisti, and A. C. Hirst, 2001: Footprinting: A seasonal connection between the tropics and mid-latitudes. *Geophys. Res. Lett.*, **28**, 3923–3926.
- , —, and —, 2003a: The seasonal footprinting mechanism in the CSIRO general circulation models. *J. Climate*, **16**, 2653–2667.
- , J. M. Wallace, and S. Battisti, 2003b: The seasonal footprinting mechanism in the Pacific: Implications for ENSO. *J. Climate*, **16**, 2668–2675.
- , M. Alexander, and A. Fontaine, 2009: Mid latitude excitation of tropical variability in the Pacific: The role of thermodynamic coupling and seasonality. *J. Climate*, **22**, 518–534.
- Walker, G. T., and E. W. Bliss, 1932: World weather V. *Mem. Roy. Meteor. Soc.*, **4**, 53–84.
- Wang, C., and J. Picaut, 2004: Understanding ENSO physics—A review. *Earth's Climate: The Ocean–Atmosphere Interaction, Geophys., Monogr.*, Vol. 147, Amer. Geophys. Union, 21–48.
- Wittenberg, A. T., 2009: Are historical records sufficient to constrain ENSO simulations? *Geophys. Res. Lett.*, **36**, L12702, doi:10.1029/2009GL038710.
- Yuan, X., 2004: ENSO-related impacts on Antarctic sea-ice: A synthesis of phenomenon and mechanisms. *Antarct. Sci.*, **16**, 415–442.
- Zhang, L., P. Chang, and L. Ji, 2009: Linking the Pacific meridional mode to ENSO: Coupled model analysis. *J. Climate*, **22**, 3488–3505.
- Zhang, Y., J. M. Wallace, and D. S. Battisti, 1997: ENSO-like interdecadal variability: 1900–93. *J. Climate*, **10**, 1004–1020.
- Zhong, Y., Z. Liu, and R. Jacob, 2008: The origin of Pacific decadal variability in the NCAR–CCSM3. *J. Climate*, **21**, 114–133.